

Microstructure observations of the summer-to-winter destratification at a coastal site in the Gulf of Naples.

Florian Kokoszka¹, Fabio Conversano¹, Daniele Iudicone¹, Bruno Ferron²,
Pascale Bouruet-Aubertot³, Justine Mc Millan⁴

¹Stazione Zoologica Anton Dohrn, Naples, Italy

²Univ. Brest, CNRS, IFREMER, IRD, Laboratoire d'Océanographie Physique et Spatiale (LOPS),

IUEM, Plouzané, France

³Sorbonne Université (UPMC, Univ Paris 06)-CNRS-IRD-MNHN, LOCEAN, Paris, France

⁴Rockland Scientific International Inc., Victoria, Canada

Key Points:

- The seasonal cycle of the dissipation rates of turbulent kinetic energy ϵ at a mid-latitude coastal site is presented, covering the destratification period.
- A progressive deepening of the mixed layer depth was observed from September to December, finally extending to the whole water-column at the beginning of winter.
- The statistics of ϵ depend upon the time of the year and the position with respect to the mixed layer depth. A seasonal increase in storminess is correlated with an increase in intermittency of the turbulence in the mixed layer.
- We observed a quadratic relation between kurtosis and skewness for the statistics of ϵ .
- A co-location of patches of higher ϵ with the shear maxima of the two first baroclinic modes suggests internal waves activity plays a role in the setting the mixing intensity despite the lack of tidal forcing.
- The low-passed microstructure shear distribution seems to support this hypothesis despite possible signal contaminations.
- The variability of the stratification is ruled by several physical processes, including freshwater inputs from land, whose importance varies with the seasons; this succession has to be considered when studying the impact of climate change upon the stratification.

Corresponding author: Florian Kokoszka, florian.kokoszka@szn.it

Abstract

A dissection of the physics of the seasonal cycle of the oceanic upper layer stratification is necessary to improve climate predictions and to constrain the response of biogeochemical cycles to the climate change. Here we present a time series of vertical profiles of ϵ , the dissipation rate of turbulent kinetic energy, obtained from a microstructure profiler at a mid-latitude 75m-deep coastal site covering the destratification occurring during the summer-to-winter period. The main signature of the destratification is a progressive deepening of the mixed layer depth (MLD) from September to November, that extended to the water-column's bottom at the beginning of winter. By grouping the data into temporal and vertical bins we found that the statistics of ϵ depend upon the time of the year and the position with respect to the MLD. A seasonal increase in storminess is correlated with the increase in intermittency of the turbulence in the mixed layer. A co-location of patches of higher ϵ with the shear maxima of the two first baroclinic modes suggests internal waves activity plays a role in setting the mixing intensity despite the lack of tidal forcing. The low-passed microstructure shear distribution seems to support this hypothesis despite possible signal contaminations. The actual origin of these energetic motions remains to be investigated. Overall, this study confirms that the variability of the stratification is ruled by several physical processes whose importance varies with the seasons. Predicting a change in stratification thus requires tackling the challenge of understanding and parameterising these processes.

Plain Language Summary

Numerical models predict an augmentation in the intensity of the stratification of the oceans due to climate change, impacting the stability of currents and the vertical supply of nutrients. These are regulated by several processes such as the ocean-atmosphere exchange of heat and freshwater, or the storms and tides generating vertical motions that can propagate, intermittently break, and induce local mixing. The intensity of each process varies with the seasons, and stratification change can be due to co-occurrences contributing diversely during time. Disentangling them with time series is thus crucial to improve the understanding of the seasonal cycle of the turbulence and make reliable predictions. Here we present a new survey describing the stratification change from summer to winter at a coastal site in the Mediterranean Sea. We found that the turbulence characteristics vary with depth and season together with the layer structure of the water column. We also observed the signature of mixing events occurring below the homogeneous layer that could be related to a recently proposed mechanism. Our study confirms the complex interplay of the processes regulating the stratification and the urgent need of long, purposely designed time series.

1 Introduction

The stratification of the oceans, that is, the density change with depth, regulates the physical processes taking place from the surface to the bottom (Garrett et al. [1978], de Boyer Montégut et al. [2004]). Its vertical structure, related to the vertical structure of temperature and salinity, results from the transfer of energy of large-scales forcings (e.g., winds, sea-air and ice-air buoyancy exchanges, tides) toward small dissipative scales (Wunsch & Ferrari [2004], Thorpe [2005]).

The transfer of energy occurs via a large variety of phenomena (e.g., internal waves, eddies, filaments, overturns Ferrari & Wunsch [2009]), whose roles are not perfectly disentangled. In addition, forcing sources may be remote. These different processes are regulated by the stratification which, in turn, is modified through the microscale mixing they ultimately provide (Brainerd & Gregg [1995], Mackinnon & Gregg [2005]). As discussed in Somavilla et al. [2017], the link between surface forcing and stratification is made more complex by the preconditioning role that surface forcing have on the permanent pycn-

80 ocline. In a context of data analyses (Guancheng et al. [2020]) and projections that indicate that global warming leads to stronger stratification (Skirris et al. [2014], Hegerl et al. [2015], Zika et al. [2015], Pastor et al. [2018]), it is of importance to identify which processes that regulate the stratification are the most sensitive to changes.

84 More generally, the relative importance of specific physical processes acting on the vertical distribution of temperature and salinity strongly varies during the year, leading to an important seasonality of the interplay of fine-scale processes over the vertical dimension (Brody et al. [2014]). The seasonal conditioning of the water column stratification regulates also the biological activity since it controls the vertical transfer and uptakes of nutrients (Sverdrup [1953], Kjørboe & Mackenzie [1995]), while several marine species take advantage or are limited by the water motions modulated by the stratification (Mann & Lazier [1996], Prairie et al. [2012], Barton et al. [2014], Wheeler et al. [2019]). Understanding its seasonality is thus relevant for the biogeochemicals cycles, harmful algae blooms and plastic dispersal, among others (Sverdrup [1953], Pingree et al. [1976], Wihsgotta et al. [2019]).

95 Fine-scale and micro-scale observations through dedicated high resolution profilers have multiplied since the first designs of microstructure probes in the 1960's (Osborn [1998], Lueck et al. [2002], Shang et al. [2016]) to better understand how energy transfers toward small scales (in the ocean). But the difficulty of the deployment at sea and the complexity of the physical phenomena to be sampled make an in situ characterization challenging. Thus, an effort toward the acquisition of high quality data at all scales, from the open ocean to the coastal area, remains a primer. Additionally, once acquired the data interpretation remains difficult since it is not always possible to disentangle the role of single processes as pointed also by the recent study of Lozovatsky et al. [2017].

104 Here we present a unique attempt to describe the seasonal cycle of the vertical stratification and associated mixing with high-resolution data collected from July 2015 to February 2016. These observations contribute to the Long Term Ecosystem Research Marechiarà (LTER-MC) initiative that produced a historical time series of a Mediterranean coastal ecosystem through a weekly sampling of the water column started in 1984 and running until now (Ribera d'Alcalá et al. [2004], Zingone et al. [2019]). The sampling site is located on the inner shelf of the Gulf of Naples, a mid-latitude gulf in the Western Mediterranean Sea having subtropical regime and almost no tides (**Fig. 1**). The shallow semi-enclosed basin presents a marked salinity contrast due to the combination of the salty Tyrrhenian Sea waters, entering from on its southern side, with the freshwater inputs from a densely inhabited coastal area on its northern part and from nearby rivers (Cianelli et al. [2012], Cianelli et al. [2017]). Forced also by recurrent, highly seasonal intense wind forcing events, its cross-shore exchanges are modulated by mesoscale eddies and sub-mesoscale filaments (Iermano et al. [2012]). The important role of lateral transport of freshwater in setting the stratification implies also that long term changes are possibly impacted also by the effects of climate change on the surrounding territories, which include regions with important winter snow accumulations. Thus, the study area is an ideal site to study how coastal salinity and temperature changes combine in setting the variability of the vertical stratification (Woodson [2018]), in a context of rising air and sea temperatures and of intensifying extreme events such as storms, floods and even, recently, Mediterranean hurricanes (Volosciuk et al. [2016], Koseki et al. [2020], W. Zhang et al. [2020]).

125 For this purpose, we will present first the hydrology obtained from the Conductivity–Temperature–Depth (CTD) measurements to depict the vertical structure of the water-column during the seasonal cycle at the coastal area. To identify the drivers of the de-stratification during the seasonal cycle, we will then investigate the timing and intensity of wind stress and buoyancy fluxes during the course of the mixed layer depth deepening weeks after weeks. Internal layers susceptible to intermittent diffusive convection and double diffusion regimes will be investigated as they may be impacted by changes in vertical stability due to surface forcings. We will describe then the occurrence of a bot-

133 tom turbid layer. Finally, we will present the seasonal cycle of the turbulent kinetic en-
 134 ergy dissipation rates obtained from vertical microstructure profiles, and describe their
 135 characteristics following the statistical framework of Lozovatsky et al. [2017]. We will
 136 conclude by depicting a conceptual scheme that illustrates the processes possibly at work
 137 during the summer-to-winter transition.

138 2 Materials and Methods

139 2.1 Hydrology and mixed layer depth (MLD)

140 Conductivity–Temperature–Depth (CTD) profiles were carried out at the LTER-
 141 MC sampling point in the Gulf of Naples (**Fig. 1**) with a Seabird **SBE-911+** mounted
 142 on a 12-bottle carousel, with all sensors calibrated. The raw 24 Hz profiles were processed
 143 using the Seabird data processing SeaSave 7.26.7 to obtain 1-m bin-averaged data. The
 144 weekly survey refers to the casts MC1160 to MC1190 and includes a total of 31 CTD
 145 profiles (supplementary Tab. S1). Independent to these data, the vertical microstruc-
 146 ture profiler (VMP-250 from Rockland Scientific International Inc, henceforth referred to
 147 as Rockland) used in this study was equipped with a nose-mounted high-precision conductivity-
 148 temperature sensors (micro-CT) from JFE Advantech, sampling at 64 Hz. These data
 149 were averaged on a regular vertical grid of 10 cm, and allowed us to collect a second hy-
 150 drological dataset, directly co-located with the microstructure measurements. CTD data
 151 were used to provide a general view on the hydrological context of our study (periods
 152 of external forcings, mixed layer depth, vertical internal layers of the water-column), and
 153 micro-CT data to infer the Turner’s regimes (see Section 2.2). For both datasets, the Gibbs-
 154 SeaWater Oceanographic Toolbox (McDougall & Barker [2011]) was used to calculate
 155 the conservative temperature T_C ($^{\circ}\text{C}$), the absolute salinity S_A (g kg^{-1}), the water den-
 156 sity ρ (kg m^{-3}), the potential density σ_0 (kg m^{-3}), the potential temperature θ_0 ($^{\circ}\text{C}$),
 157 and the Brunt-Väisälä frequency N^2 (s^{-2}). When mentioned thereafter, T and S refer
 158 to T_C and S_A . Mixed layer depth (MLD, m) was calculated following the method of de
 159 Boyer Montégut et al. [2004] based on threshold values. Given a vertical profile of den-
 160 sity $\sigma_0(z)$, or potential temperature $\theta_0(z)$, we calculated the depth below $z_{ref} = 3 \text{ m}$,
 161 where the profile reached thresholds defined as a cumulative of 0.4°C for θ_0 , and 0.03 kg m^{-3}
 162 for σ_0 . The VMP was also equipped with a fluorometer-turbidity sensor from JFE Ad-
 163 vantech, sampling at 512 Hz. These data were converted to physical units using the ODAS
 164 Matlab Toolbox provided by Rockland (version 4.4.06). The sensor has a spatial response
 165 of $\sim 1 \text{ cm}$ (Wolk et al. [2002]) and the data were averaged over 10 cm. A mean value of
 166 -2.5 FTU over the whole cast was taken as a reference to establish a ΔFTU and iden-
 167 tify turbid layers in the water-column.

168 2.2 Turner’s regimes

169 We applied the method introduced by Turner (Turner [1967], [1973]) to localize parts
 170 of the water column where vertical gradients of T and S are favourable to double-diffusive
 171 instability. The high-resolution CT data from the JFE Advantech sensor mounted on
 172 the VMP-250 was used for this analysis. Combining the vertical gradients and their signs
 173 allows the identification of stability regimes, that can be defined from the ratio $R_\rho =$
 174 $(\alpha d\theta/dz)/(\beta dS/dz)$ where $\alpha = -\rho^{-1}(d\rho/d\theta)$ is the thermal expansion coefficient, $\beta =$
 175 $\rho^{-1}(d\rho/dS)$ is the haline contraction coefficient, where $d\rho/dz$ and $d\theta/dz$ are the verti-
 176 cal gradients of density and temperature, respectively. This ratio is used to calculate the
 177 Turner angles ($^{\circ}$) $Tu = \arctan((1 + R_\rho)/(1 - R_\rho))$ (Ruddick [1983]). The value of the
 178 Turner angle defines various stability regimes. A diffusive convection regime (e.g., fresh
 179 cold layers over warm salty layer) arises when $-90^{\circ} < Tu < -45^{\circ}$. A double-diffusive
 180 regime (e.g., salty warm layer over cold fresh layer) arises when $45^{\circ} < Tu < 90^{\circ}$. Within
 181 each of these regimes, the instability is higher when $|Tu|$ is close to 90 degrees. A sta-

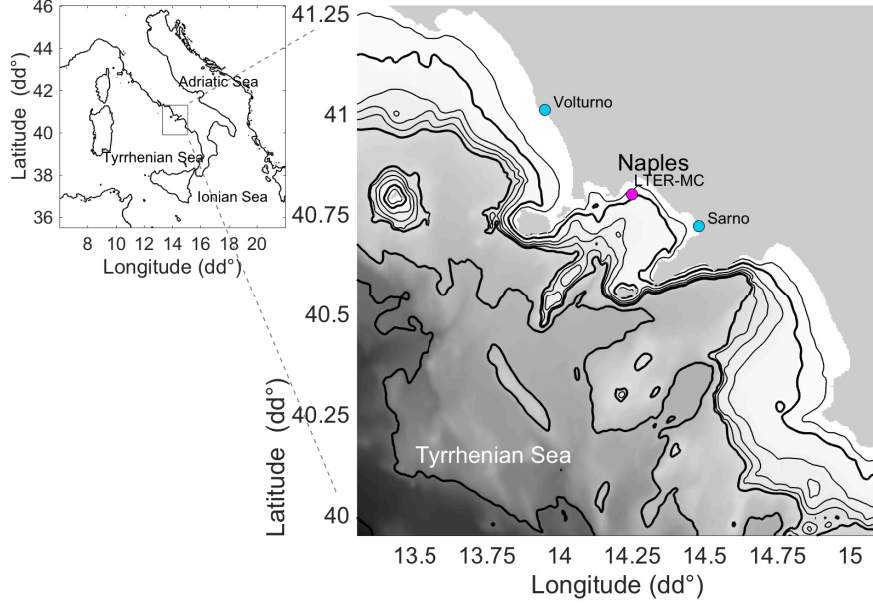


Figure 1: Bathymetry of the Gulf of Naples (GEBCO grid [GEBCO, 2020]) along the Tyrrhenian Sea in the Mediterranean basin). The 75m-deep LTER-MC coastal sampling site ($14.25^{\circ}E$, $40.80^{\circ}N$) is located by the pink dot. Volturno and Sarno’s river mouths are shown in blue. Thin lines indicate the 50, 200, 300 and 400 m isobaths, thick ones indicate the 100, 500, 1000 and 2000 m isobaths.

182 ble regime occurs when $|Tu| < 45^{\circ}$, whereas a gravitationally unstable regime occurs
 183 when $|Tu| > 90^{\circ}$.

184 2.3 Heat fluxes, winds and precipitations

185 Surface heat fluxes (latent and sensible, with net solar and thermal radiation, in
 186 $W m^{-2}$), wind velocities (U_{10} and V_{10} , $m s^{-1}$), evaporation E and precipitation rates P
 187 ($mm d^{-1}$) were extracted from the ERA5 re-analysed product provided by Copernicus
 188 (ERA5(C3S) [2017]). The closest grid-point was selected from the LTER-MC geographi-
 189 cal position ($14.25^{\circ}E$ and $40.80^{\circ}N$), with a 6-hour temporal resolution, over the whole
 190 period. We used those values to infer the Monin-Obukhov length scale (L_{MO}) (Obukhov
 191 [n.d.], Obukhov [1971]), a critical length scale describing the depth at which the turbu-
 192 lence is generated more by wind shear than buoyancy forcings, defined as $L_{MO} = u_*^3 / \kappa B$
 193 (m). Here u_* is the friction velocity of the wind ($m s^{-1}$), κ the von Karman’s constant
 194 (here 0.4), and B the buoyancy flux ($m^2 s^{-3}$), defined such that $B > 0$ if stabilizing the
 195 water-column. Buoyancy flux is proportional to the density flux at the surface, as $B =$
 196 gQ_p / ρ_0 , where the density flux Q_p into the ocean from the atmosphere was computed
 197 as (H.-M. Zhang & Talley [1998]) $Q_p = \rho(\alpha F_T + \beta F_S)$, with α and β the thermal ex-
 198 pansion and saline contraction coefficients, respectively. Here $F_T = -Q_{net} / \rho_{sea} C_p$, and
 199 $F_S = (E - P)S / (1 - S/1000)$, where C_p is the specific heat of sea water, E , P , and S
 200 are the evaporation, precipitation and sea surface salinity. The net radiative heat flux
 201 at the ocean surface Q_{net} ($W m^{-2}$) was calculated from the combination of the incom-
 202 ing short wave, net incoming and emitted long wave, sensible and latent heat. The ve-
 203 locity friction u_* was calculated as $u_* = \sqrt{\tau / \rho_{sea}}$, where ρ_{sea} is the density of sea wa-
 204 ter, and τ the wind stress, as $\tau = \rho_{air} C_D U_{10}^2$, where $\rho_{air} = 1.22 kg m^{-3}$, and drag co-

205 efficient C_D and velocity at 10 m U_{10} calculated from wind velocity following Large &
 206 Pond [1981]. Different regimes can be identified from the L_{MO} diagnostic : wind stress
 207 dominance over stable B ($L_{MO} > 1$), stable B dominating the wind stress ($0 < L_{MO} <$
 208 1), wind stress dominating a destabilising B ($L_{MO} < -1$), and a destabilising B dom-
 209 inating wind stress ($-1 < L_{MO} < 0$).

210 2.4 Microstructure data

211 Microstructure measurements were collected at the LTER-MC point using a VMP-250
 212 profiler from Rockland. During each deployment, between one and four profiles were com-
 213 pleted down to five meters above the bottom (75 m deep), resulting in a total of 71 pro-
 214 files among the 31 weekly CTD profiles of the survey (supplementary Tab. S1). The pro-
 215 filer was deployed with a tether from the ship and fell quasi-freely at a speed of 0.7 m s^{-1}
 216 to 0.9 m s^{-1} . The profiler was equipped with two microstructure shear sensors, a fast re-
 217 sponse temperature sensor (FP07) and a micro-conductivity sensor (SBE7), which were
 218 all sampled at 512 Hz. The shear probes measured the vertical shear of horizontal ve-
 219 locity fluctuations (i.e. du/dz , dv/dz). The raw signals are subject to noise and signal
 220 contamination from instrument vibrations, internal circuitry, and impact of biology and
 221 sediment. To reduce the impact of signal contamination, several processing steps were
 222 required before computing the spectra and dissipation rate. Firstly, the upper and lower
 223 meters of each cast, where the profiler was accelerating and decelerating, were discarded.
 224 These segments were identified and removed manually when the profiling speed deviated
 225 from the median value by more than ± 1.5 times the standard deviation. Secondly, large
 226 amplitude, short-duration spikes were eliminated from the shear data using the despik-
 227 ing algorithm provided in Rockland’s ODAS Matlab Library (v4.4.06). In particular, spikes
 228 were identified using a threshold value of 5 when comparing the instantaneous shear sig-
 229 nal to a smoothed version. The smoothed signal was obtained using a first-order But-
 230 terworth filter, with a cut-off frequency ranging from 0.7 to 0.9 Hz, depending on the me-
 231 dian value of the fall speed. Once identified, spikes were removed over a 5 cm segment
 232 (ca. 0.07 s). Thirdly, the shear signals were high-pass filtered at 1.5 Hz to remove low-
 233 frequency contamination (0.1 - 1 Hz) that is believed to be associated with the pyroelec-
 234 tric effect. The spectrum of the high-passed vertical shear signal was computed and used
 235 to estimate the dissipation rate (see below). The low-frequency portion of the signal, i.e.
 236 Sh_{LP} , from shear probe 1 was also analyzed (see Appendix).

237 2.5 Dissipation rate

238 The dissipation rate of turbulent kinetic energy (TKE) was calculated using the
 239 isotropic relation $\epsilon = 7.5\nu\langle(\frac{\partial u}{\partial z})^2\rangle = 7.5\nu\langle(\frac{\partial v}{\partial z})^2\rangle$, where ν is the kinematic viscosity
 240 of seawater and u and v are the horizontal components of the small-scale velocity fluc-
 241 tuations. In practice, the estimate of ϵ was obtained iteratively by integrating the shear
 242 spectra up to an upper wavenumber limit (k_{\max}), i.e. $\epsilon = 7.5\nu \int_0^{k_{\max}} \phi(k)dk$ as is out-
 243 lined in Rockland’s Technical Note 028 (Lueck [2016]). This was done for each microstruc-
 244 ture sensor separately, i. e. for du/dz (as sh_1) and dv/dz (as sh_2). The shear spectra,
 245 and hence dissipation rates, were estimated using the ODAS Matlab Library (v4.4.06).
 246 Dissipation segment lengths of 3 s were used with 1 s fft-segments that overlapped by 50%.
 247 The dissipation segments themselves were overlapped by ca. 1.5 s, which resulted in a
 248 vertical resolution in ϵ of approximately 1.2 m. Contamination of the spectra for instru-
 249 ment vibrations was reduced using the cross-coherency method of Goodman et al. [2006].
 250 The quality of the spectra were assessed using a figure of merit, which is defined as $FM =$
 251 $\sqrt{dof} \times mad$, where $dof = 9.5$ is the number of degrees of freedom of the spectra (Nut-
 252 tall [1971]) and mad is the mean absolute deviation of the spectral values from the Nas-
 253 myth spectrum as $mad = \frac{1}{n_k} \sum_{i=1}^{n_k} |\frac{\phi(k_i)}{\phi_{Nasmyth}(k_i)} - 1|$ where n_k is the number of discrete
 254 wavenumbers up to k_{\max} (Ruddick et al. [2000]). Segments of data where the spectra
 255 had $FM > 1.5$ were rejected from further analysis. The final dissipation rate was ob-

256 tained by averaging the estimates for the two independent probes, i.e. ϵ_1 and ϵ_2 (respec-
 257 tively from sh_1 and sh_2). If the values of ϵ_1 and ϵ_2 differed by more than a factor of 10,
 258 the minimum value was used. FM values and Nasmyth's fit are included in the Fig. S1
 259 of the Supplementary information. Probability distribution functions (pdfs) of ϵ were
 260 computed with the Matlab Statistical Toolbox. Pdfs were obtained over various tempo-
 261 ral and depth bins covering the physical domain of external forcings and vertical layers.

262 3 Results

263 3.1 Hydrology from the CTD profiles

264 The Gulf of Naples (**Fig. 1**) stands as a non-tidal coastal area in the Western Mediter-
 265 ranean marked by a subtropical regime, and is directly affected by continental freshwa-
 266 ter runoffs and salty water from the Tyrrhenian Sea.

267 We present on **Fig. 2.a** the hydrology of the water-column during our survey. A
 268 clear seasonal cycle is visible : a stratified period in July-August, followed by a progres-
 269 sive deepening of the MLD from September to November, that finally reaches a period
 270 when the water-column can be considered as fully mixed, from December to February.
 271 From the surface down to 50-60 m depth, relatively fresh waters persist all along the sum-
 272 mer till early November after which they are rapidly replaced by salty waters that re-
 273 main till the end of the record (**Fig. 2.a**).

274 A salty bottom layer of 38.1 to 38.3 g kg^{-1} is visible below the 28.3 kg m^{-3} isopy-
 275 cnal layer all along the record. As for the general pattern of the Brunt-Väisälä frequency
 276 N^2 (**Fig. 2.b**), a strongly stratified, 10 m thick transitional layer is observed below the
 277 MLD, separating the surface from the internal and bottom layers (Johnston & Rudnick
 278 [2009]). To identify the physical processes acting below the MLD, we partitioned the col-
 279 umn into layers using a vertical decomposition into baroclinic modes 1 and 2 (see Sup-
 280 plementary information S2), denoted by B1 and B2 respectively. The determination of
 281 their vertical extension was made for each profile by identifying the depth ranges con-
 282 taining the shear maximum values. The maxima of B1 are located immediately below
 283 the MLD and are associated with the highly stratified part of the water column, while
 284 the maxima of B2 lie deeper and are associated with a weaker stratification (see suppl-
 285 ementary Fig. S2). Finally, the water column between B2 and the bottom was consid-
 286 ered as a separate layer. We present the vertical extension of the vertical bins in **Fig.**
 287 **2.c**. This partitioning was then used for the statistical characterization of the destrati-
 288 fication.

289 3.2 Buoyancy fluxes and wind forcings

290 The time evolution of buoyancy fluxes and surface winds is investigated to look for
 291 possible impacts on the deepening of the MLD. In general, positive buoyancy fluxes strenght-
 292 ened the stratification of the water column while negative buoyancy fluxes weakened the
 293 stratification and may lead to surface convection and deepening of the MLD. During sum-
 294 mer and till mid-September, the daily averaged B was always positive apart from three
 295 short episodes of negatively buoyant days (**Fig. 3.a**, gray line). In contrast, after mid-
 296 September B remained negative (or close to zero). Consequently, from the beginning of
 297 the observed period, the cumulative buoyancy flux increases and reaches a maximum level
 298 around mid-September and then constantly decreases from mid-October to reach a min-
 299 imum at the end of the record (**Fig. 3.a**, gray dashed line). The contribution of heat
 300 (B_T) and freshwater (B_S) fluxes to daily buoyancy fluxes clearly show that B_T domi-
 301 nates, being larger than B_S by one order of magnitude except during rain events (**Fig.**
 302 **3.a** and **Fig. 3.b**, blue lines). Precipitation rates shows intermittent events with val-
 303 ues larger than 20 mm d^{-1} , with a maximum of about 70 mm d^{-1} in early October, fol-
 304 lowed by intermittent rainy events during the rest of the period. During those events,

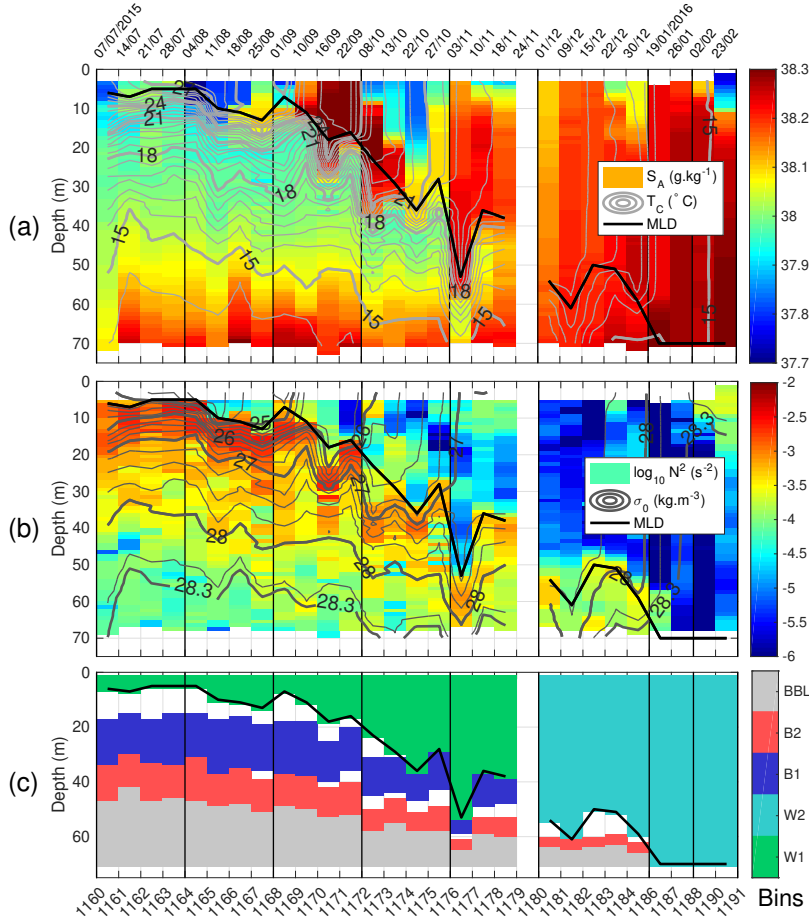


Figure 2: CTD SBE-911+ profiles. (a) Absolute Salinity S_A (g kg^{-1}) with contours of Conservative temperature T_C ($^{\circ}\text{C}$). (b) Brunt-Väisälä frequency N^2 (s^{-2}) and contours of potential density σ_0 , plotted from 24 to 27 kg m^{-3} every 0.25 kg m^{-3} , with the 28.3 kg m^{-3} isopycnal emphasized in thick black near the bottom. (c) Vertical and temporal bins used thereafter for the statistical characterization by periods and layers: surface to MLD during the summer to autumn period $W1$ (green), surface to MLD during the winter period $W2$ (cyan), the vertical layer of the shear maxima of the first baroclinic mode $B1$ (blue) and second baroclinic mode $B2$ (red), and the bottom boundary layer BBL (gray). (All) $MLD_{\theta^0.4}^C$ (thick black line). X-axis indicates the sequence of MC-CTD profiles references, and sampling dates are given on the panel top.

305 (positive) B_S became comparable to B_T (**Fig. 3.a**, solid pink blue and gray lines). Note
 306 that without measurements of the river runoffs contribution, there were not accounted
 307 for despite they are likely of importance over this coastal area (the Sarno river runoff into
 308 the Gulf of Naples is about $13 \text{ m}^3 \text{ s}^{-1}$, while the Volturno river runoff into the Gulf of
 309 Gaeta is about $82 \text{ m}^3 \text{ s}^{-1}$ (Albanese et al. [2012])).

310 Buoyancy fluxes counteract the wind stresses, which are able to mechanically mix
 311 the surface layer and contribute to the deepening of the MLD. The wind stress (**Fig. 3.b**)
 312 over the summer period is weak and shows few intermittent events before the mid-September
 313 (MC1171) with $u_*^3 < 0.5 \times 10^{-6} \text{ m}^3 \text{ s}^{-3}$. Stronger energetic storms with values $> 1.5 \times 10^{-6}$
 314 $\text{m}^3 \text{ s}^{-3}$ occurred two months later, around the 20th November, followed in January and
 315 February by other stormy periods. To identify the direct contribution of the wind to the

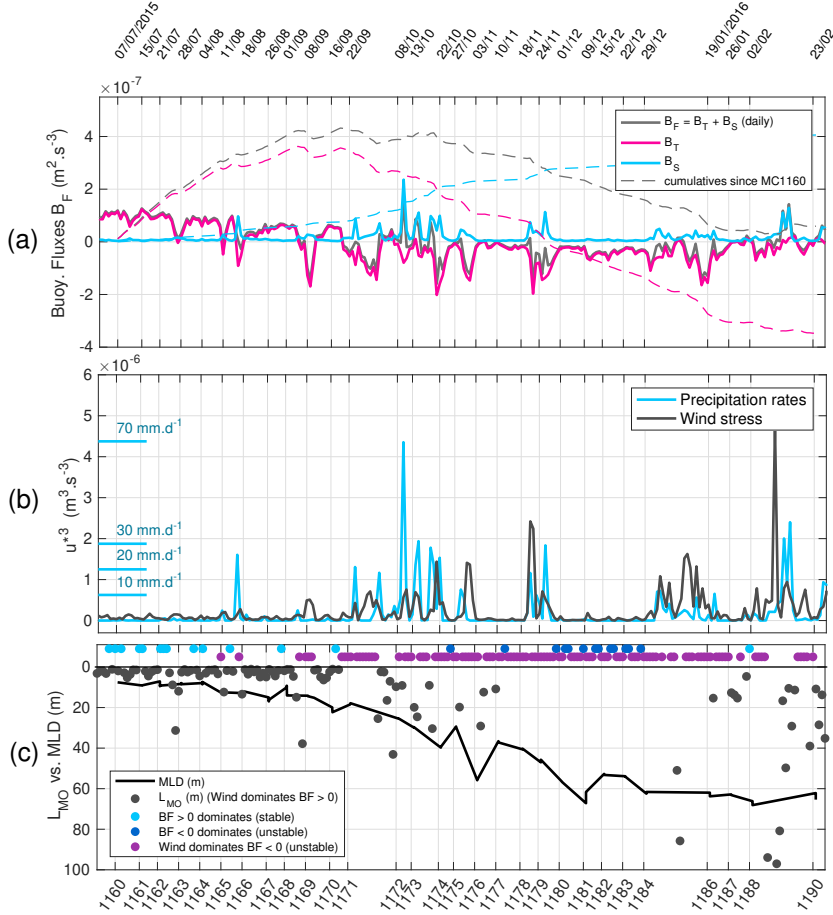


Figure 3: (a) Daily averaged buoyancy fluxes B ($\text{m}^2 \text{s}^{-3}$). Gray line indicates the sum of heat and freshwater contributions B_T (solid pink) and B_S (solid blue). The associated dashed lines indicate the cumulative values from the 7th of July 2015 (scaled down by a factor 10 for graphical purposes). (b) Daily averaged precipitation rates P ($\text{mm} \text{d}^{-1}$ in blue) and wind stress u_*^3 ($\text{m}^3 \text{s}^{-3}$ in gray). (c) MLD (solid black) and Monin-Obhukov length scale L_{MO} (m in gray dots) during stable buoyancy fluxes. On the horizontal line near surface, dots indicate the occurrences of the other regimes (stable in light blue, unstable dominated by negative fluxes in dark blue, and unstable fluxes dominated by wind stress in purple). X-axis indicates the MC-CTD casts references. Sampling dates are given on the panel top.

316 mixing within the water column, we calculated the Monin-Obhukov length scale (see Meth-
 317 ods) to characterize the dominance of wind stress over positive buoyancy fluxes. Unre-
 318 realistically large values (i.e. $|L_{MO}| > 100$ m) have been discarded. Note that, because
 319 strong winds prevented any ship observation during storms, the MLD was only diagnosed
 320 after (and not during) the occurrence of extreme events, inhibiting a detailed analysis
 321 of covariance between MLD and L_{MO} during stormy periods.

322 We show on **Fig. 3.c** (gray dots) cases when wind mechanical forcing was respon-
 323 sible for the MLD deepening. During the stratified period, the L_{MO} remained in the range
 324 of 0.01 – 1m, that is, the winds were too weak to break the stratification and thus to
 325 deepen the MLD (MC1160 to MC1170 included, from July to mid-September). Strong
 326 values of $u_*^3 > 0.5 \times 10^{-6} \text{ m}^3 \text{ s}^{-3}$ occurred after MC1171, after which the L_{MO} regime

327 shifted toward values $O(10\text{ m})$ until MC1177 included (mid-November). The strong event
 328 of $u_*^3 > 2 \times 10^{-6} \text{ m}^3 \text{ s}^{-3}$ of the end of November between MC1178 and MC1179 marked
 329 the start of the winter period, with values of L_{MO} reaching values $> 10\text{ m}$ between MC1184-
 330 MC1186 and MC1188-MC1190. Most of the MLD deepening occurs during the period
 331 from late-summer to winter. Despite this period is characterized by negative buoyancy
 332 fluxe, our analysis clearly shows that wind forcings dominates over B (**Fig. 3.c**, purple
 333 points) rather than the opposite (dark blue dots). Thus, the MLD deepening is mostly
 334 induced by wind mechanical mixing. Cases with no significant wind conditions occurred
 335 mainly in December, with some additional short events in October and November.

336 This change of the main atmospheric forcings properties over the seasons led us to
 337 split the analysis of two temporal periods : $W1$ from MC1160 to MC1178 (July to mid-
 338 November), and $W2$ from MC1179 to MC1190 (end of November to February), respec-
 339 tively (**Fig. 2.c**).

340 3.3 Turner's regimes : diffusive convection and double diffusion

341 The seasonal variability we observed is associated with large variations of the ther-
 342 mohaline vertical gradients that may drive various regimes of stability. We quantify those
 343 different regimes through the study of Turner's angles, estimated from the relative con-
 344 tribution of vertical gradients of salinity and temperature (Section 2.2). There is a clear
 345 partition of the stability between diffusive convection and salt fingering regimes at the
 346 MLD (**Fig. 4.a**). In the fall and winter months, the diffusive convection regime occu-
 347 pies the region above the MLD, whereas in the summer months the salt-fingering regime
 348 is present beneath the ML. More complete statistics of the Turner angles are presented
 349 in supplementary Tab. S2. Diffusive convection regime is observed locally with patchy
 350 structures that appeared in August at the surface, followed by larger ones in October,
 351 between 10 and 30 m . This situation repeated in December, although the vertical dis-
 352 tribution of this regime is more variable. Below the ML, a pattern of double diffusive
 353 regime is visible, driven by warm and salty water overlaying on the relatively colder and
 354 cooler layers. The period from mid-September to November presented layers prone to
 355 salt-fingering that were located below the local maximum of salinity of 38.2 g kg^{-1} . The
 356 periods $W1$ (late summer and fall) and $W2$ (winter) presented differences in the intensi-
 357 ty of the diffusive regime, with median intensity of $Tu \approx -45^\circ$ and $R_\rho \approx 0.33$ dur-
 358 ing $W1$, weaker in term of instability than for $W2$ showing median values $Tu \approx -72^\circ$
 359 and $R_\rho \approx 0.5$. In terms of salt fingers, the regime observed in the ML during the de-
 360 stratification shows a median value of $Tu \approx 59^\circ$ and $R_\rho \approx 3.8$, which is more intense
 361 than the regime found below the MLD (median $Tu \approx 50^\circ$ and $R_\rho \approx 8.4$).

362 3.4 Turbidity observations

363 The seasonal variability of vertical mixing is associated here with some patterns
 364 visible in the turbidity measurements of the JFE Advantech Co. fluorometer-turbidity
 365 sensor mounted on the VMP-250 (**Fig. 4.b**). These data indicate a turbid bottom layer
 366 co-located with the deep salty layer (**Fig. 2.a**). When the ML reaches the proximity of
 367 the bottom, from the end of October to December, some turbid bottom patches are vis-
 368 ible (MC1175 on the supplementary Fig. S3.b, or MC1180 on Fig. S3.c). This provides
 369 evidence of the re-suspension of sediments in a non-tidal area, by energetic processes lo-
 370 cated between the MLD and the bottom boundary layer. Once a full vertical homoge-
 371 nization is achieved in January (the core of winter period), no additional turbid layers
 372 are observed. Looking at the subsurface, local turbid patches are present inside the ML
 373 from September to November, with structures occupying a large part of the water col-
 374 umn (MC1179 on **Fig. 4.b**). This depicts the complexity of the winter mixing at the
 375 coastal area, underlying the possible important role of the runoffs discharging sediments
 376 at various point of the coast, and of the mesoscale and submesoscale features laterally
 377 advecting them.

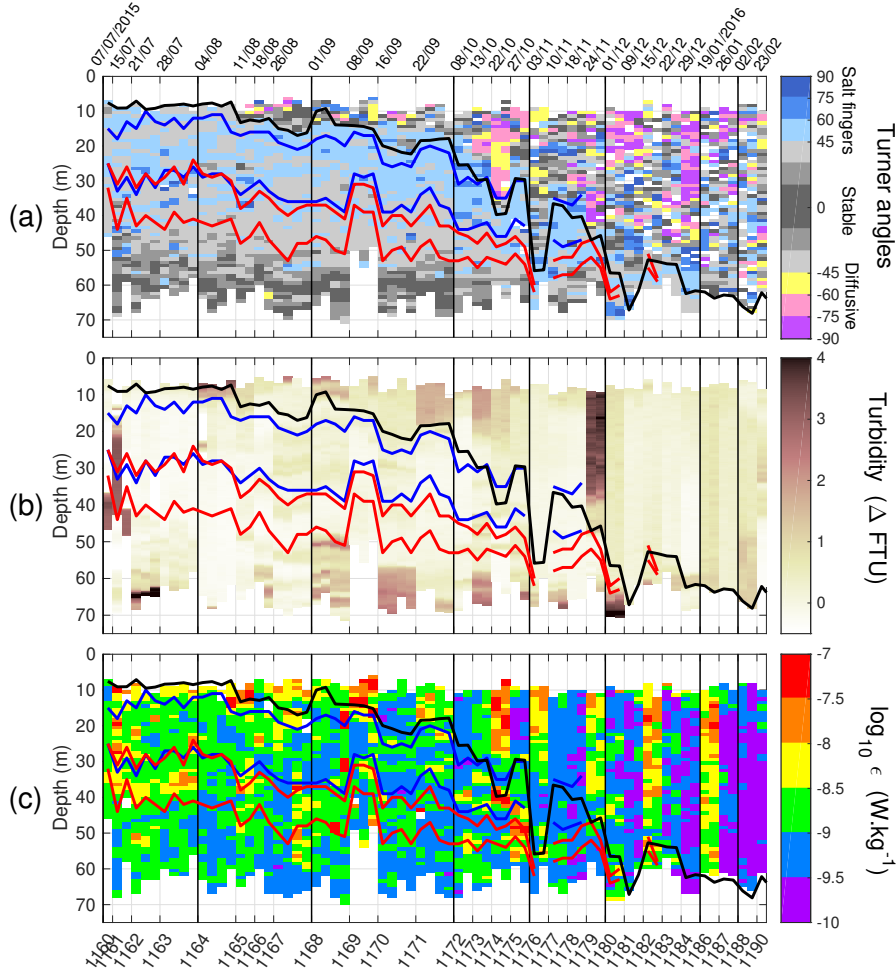


Figure 4: VMP-250 profiles, plotted sequentially (x-axis does not represent time). (a) Turner angles (angular $^\circ$), (b) Turbidity (ΔFTU) (offset from a reference value), and (c) Dissipation rate estimates ($W \cdot kg^{-1}$). (All $MLD_{\theta_0}^{0.4^\circ C}$ (thick black), region of maximum energy of baroclinic mode 1 (between blue lines) and mode 2 (between red lines). The VMP profiles are plotted sequentially along the x-axis, where the MC casts references are indicated (from one to four VMP profiles by cast). Sampling dates are given on the panel top.

378

3.5 Turbulent kinetic energy dissipation rate ϵ

379

380

381

382

383

384

385

386

387

388

The seasonal sequence of vertical profiles of dissipation rates of turbulent kinetic energy shows maximum values between 10^{-8} and $10^{-7} W \cdot kg^{-1}$ (Fig. 4.c), distributed through patches in various parts of the water column. For a given station, ϵ varies within a factor of five between the successive casts done typically within one hour (e.g., stations MC1163, MC1168, or MC1171). The summer period shows values of $10^{-8} W \cdot kg^{-1}$ at the depth-range of the MLD, around 10 m. The most intense patches are from 5×10^{-7} to $10^{-8} W \cdot kg^{-1}$ between 20 and 35 m in July (MC1160 to MC1163), then between 35 and 50 m in August and September (MC1164 to MC1171). They match the MLD depth in October (MC1174 and MC1175). Minimum values of $10^{-10} W \cdot kg^{-1}$ are measured, which are near the noise limit of the instrument. In winter, the dissipation rates are low through-

389 out most of the water column (MC1184, MC1188, MC1190). The turbid patches iden-
 390 tified previously are associated with local patches of ϵ from August to January, with val-
 391 ues from 10^{-8} to 10^{-7} W kg^{-1} in surface from 10 m to around 20 m (MC1165, MC1171,
 392 MC1174), and in the lower range of around 10^{-9} to 10^{-8} W kg^{-1} , into the water col-
 393 umn (MC1179, MC1186) or at the proximity of the bottom (MC1168, MC1173).

394 Profiles of ϵ are grouped by their mean and median values over the stratified pe-
 395 riod $W1$ and winter period $W2$ (**Fig. 5**). During $W1$, the median profiles converge from
 396 10^{-8} to 10^{-9} W kg^{-1} from 10 to 25 m, and then remains around 10^{-9} W kg^{-1} down to
 397 the bottom, punctuated by local intense values $> 10^{-7}$ W kg^{-1} . Layers below the ML
 398 show intermittent local maximum values reaching 10^{-8} W kg^{-1} , located in the vertical
 399 between region of the two first baroclinic modes maximum. The winter period $W2$ shows
 400 a tendency of $\langle \epsilon \rangle$ values to be centered around 10^{-10} and 5×10^{-8} W kg^{-1} (**Fig. 5.b**).
 401 Peaks are observed at various depths in the water-column, marking both spatial and tem-
 402 poral intermittency. They are more pronounced in the stratified layers, which may un-
 403 derline that intermittency is stronger in these locations. It should be noted that our ob-
 404 servations were made when weather conditions were favourable for a safe deployment of
 405 the VMP-250, sometimes after energetic storms but certainly never during storms. There-
 406 fore, the most intense turbulent events are likely missed.

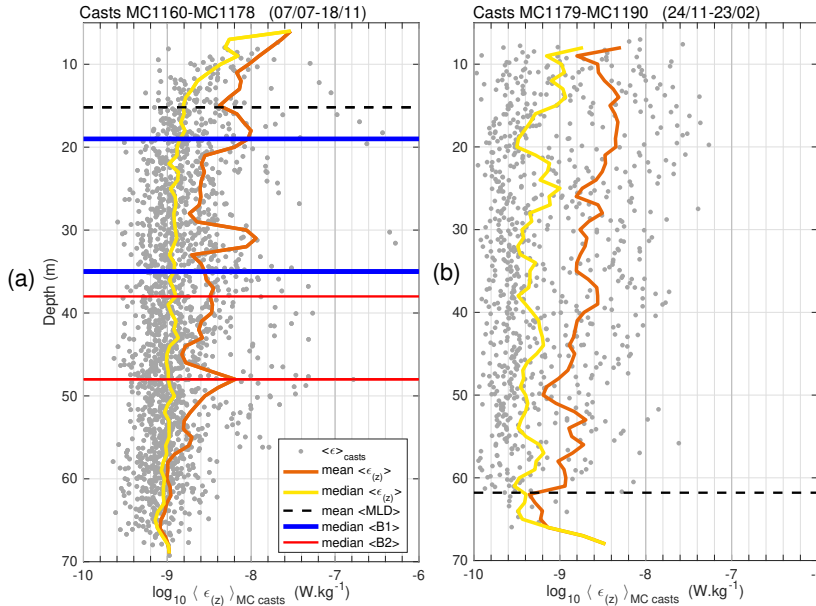


Figure 5: Mean (orange) and median (yellow) profiles of ϵ (W kg^{-1}) over the (a) summer-fall period $W1$ and (b) winter period $W2$. Gray background points are individual ϵ estimates. Horizontal dashed lines indicates the median depths of the MLD (black) and the upper and lower depths of B1 (blue) and B2 (red) during the stratified period $W1$.

407 3.6 Statistical description of ϵ and N^2

408 To characterize the distributions of ϵ , we applied the same framework as Lozovatsky
 409 et al. [2017]. We present in **Fig. 6** the empirical probability density function (pdf) of
 410 ϵ and N^2 on the two forcing periods $W1$ and $W2$, and differentiate the surface from the
 411 internal and bottom layers B1, B2 and BBL (see **Fig. 2.c**).

412 *3.6.0.1 Pdf of ϵ and N^2* The pdf for the surface bins (**Fig. 6.a**) shows values
 413 around $4 \times 10^{-10} \text{ W kg}^{-1}$ for W1, and $2 \times 10^{-10} \text{ W kg}^{-1}$ for W2, the latter being dom-
 414 inated by stronger winds and negative buoyancy fluxes. Both distribution are well fit-
 415 ted by a Burr type XII, and differ from log-normality. Regarding the stratification (**Fig.**
 416 **6.b**), the summer to fall period shows a distribution centered on $5 \times 10^{-5} \text{ s}^{-2}$ (W1 in
 417 green), while winter is characterized by a distribution centered on $3 \times 10^{-5} \text{ s}^{-2}$ (W2 in
 418 cyan). Below the mixed layers (**Fig. 6.c**), the pdf of ϵ shows a dominant peak centered
 419 on $5 \times 10^{-10} \text{ W kg}^{-1}$ for B1, and on $9 \times 10^{-10} \text{ W kg}^{-1}$ for B2. The distribution within
 420 the BBL (**Fig. 6.e**) is narrower compared to B1 and B2, and shows a dominant peak
 421 centered on $7 \times 10^{-10} \text{ W kg}^{-1}$. The observations are better described by the Burr type
 422 XII distribution than the log-normal, even if the deviation from log-normality is not so
 423 pronounced than for the distributions of the surface bins W1 and W2. Regarding the
 424 N^2 below the ML (**Fig. 6.d**), the pdf in B1 is centered around $4 \times 10^{-4} \text{ s}^{-2}$ and close
 425 to log-normality. The distribution in B2 is more variable, with values spread in the range
 426 2×10^{-5} to $3 \times 10^{-4} \text{ s}^{-2}$, making difficult to distinguish which distribution fits better.
 427 Similarly, in the BBL (**Fig. 6.f**) values are spread in a wide range (3×10^{-5} to 2×10^{-4}
 428 s^{-2}), with a central peak at $7 \times 10^{-5} \text{ s}^{-2}$, making it difficult to define a best fit between
 429 Burr and log-normal distributions. Details of statistics are given in **Tab. 1.a,b**.

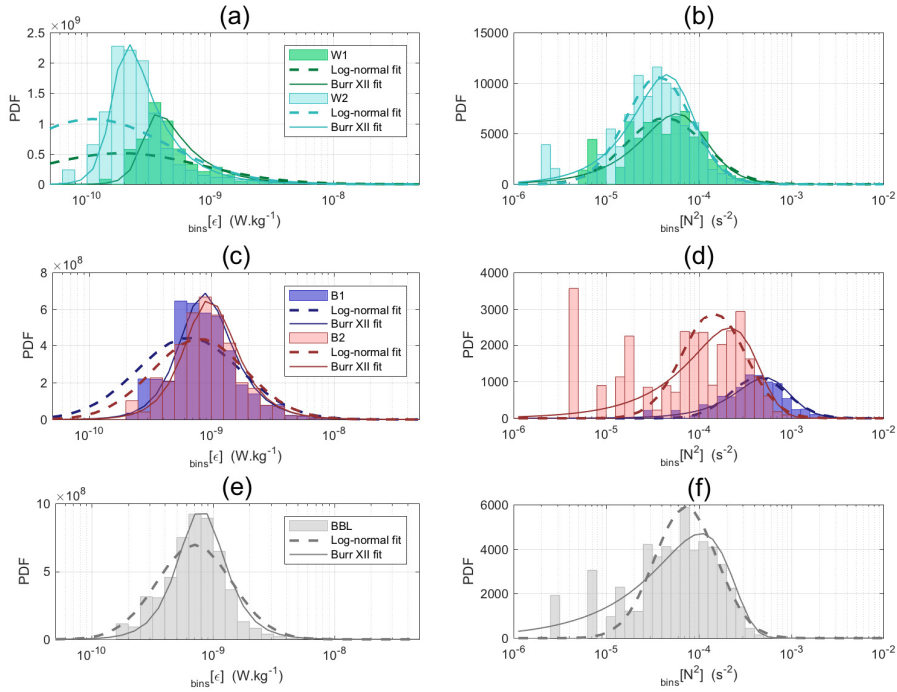


Figure 6: PDFs of ϵ (W kg^{-1}) (left), and N^2 (s^{-2}) (right), through temporal bins W1 and W2 (a,b), vertical layers B1 and B2 (c,d), and near the bottom BBL (e,f). Fits of log-normal and Burr type XII distribution are indicated with the dashed and plain black lines, respectively. Bins are shown on Fig. 2.c, and detailed statistics are given in Tab. 1.

Table 1: Statistics of ϵ (a) and N^2 (b). For both quantities are given general statistics by bins, and parameters for the fits of log-normal and Burr Type XII distributions, with their confidence intervals (c.i.). (c) Parameters of the quadratic fit $K = aS^2 + b$ of the $K = f(S)$.

(a) Statistics for ϵ

General

| Bin | N (Pop.) (by bins) | Total (All data) | % | mean | median | skewness | kurtosis |
|-----|-----------------------|---------------------|----|-----------------------|------------------------|----------|----------|
| W1 | 372 | 3084 | 12 | 5.70×10^{-9} | 1.07×10^{-9} | 5.82 | 51.58 |
| W2 | 771 | 3084 | 25 | 2.38×10^{-9} | 4.05×10^{-10} | 4.67 | 31.56 |
| B1 | 561 | 3084 | 18 | 5.23×10^{-9} | 1.23×10^{-9} | 12.33 | 162.21 |
| B2 | 379 | 3084 | 12 | 2.95×10^{-9} | 1.30×10^{-9} | 13.43 | 217.17 |
| BBL | 638 | 3084 | 21 | 1.51×10^{-9} | 9.63×10^{-10} | 7.08 | 67.67 |

Log-normal fit

| Bin | mean | median | μ | [c.i.] | σ | [c.i.] |
|-----|-----------------------|------------------------|--------|-------------------|----------|---------------|
| W1 | 4.88×10^{-9} | 1.59×10^{-9} | -20.25 | [-20.40 - -20.10] | 1.49 | [1.39 - 1.61] |
| W2 | 1.90×10^{-9} | 7.09×10^{-10} | -21.06 | [-21.16 - -20.96] | 1.40 | [1.33 - 1.48] |
| B1 | 2.38×10^{-9} | 1.48×10^{-9} | -20.32 | [-20.40 - -20.24] | 0.96 | [0.91 - 1.02] |
| B2 | 2.24×10^{-9} | 1.52×10^{-9} | -20.29 | [-20.38 - -20.20] | 0.87 | [0.81 - 0.94] |
| BBL | 1.33×10^{-9} | 1.03×10^{-9} | -20.68 | [-20.74 - -20.63] | 0.71 | [0.67 - 0.75] |

Burr XII fit

| Bin | mean | median | α | [c.i.] | c | [c.i.] | k | [c.i.] |
|-----|-----------------------|------------------------|------------------------|----------------------------------|------|---------------|------|---------------|
| W1 | Inf | 9.47×10^{-10} | 2.80×10^{-10} | [2.54 - 3.08×10^{-10}] | 7.06 | [5.03 - 9.92] | 0.08 | [0.05 - 0.11] |
| W2 | Inf | 4.56×10^{-10} | 1.60×10^{-10} | [1.50 - 1.70×10^{-10}] | 6.82 | [5.57 - 8.37] | 0.09 | [0.07 - 0.12] |
| B1 | 4.18×10^{-9} | 1.24×10^{-9} | 7.19×10^{-10} | [6.47 - 7.98×10^{-10}] | 3.98 | [3.35 - 4.72] | 0.30 | [0.23 - 0.38] |
| B2 | 3.19×10^{-9} | 1.31×10^{-9} | 8.09×10^{-10} | [7.14 - 9.15×10^{-10}] | 3.90 | [3.21 - 4.73] | 0.33 | [0.25 - 0.45] |
| BBL | 1.42×10^{-9} | 9.55×10^{-10} | 7.00×10^{-10} | [6.42 - 7.63×10^{-10}] | 3.99 | [3.51 - 4.52] | 0.46 | [0.37 - 0.57] |

(b) Statistics for N^2

General

| Bin | N (Pop.) (by bins) | Total (All data) | % | mean | median | skewness | kurtosis |
|-----|-----------------------|---------------------|----|-----------------------|-----------------------|----------|----------|
| W1 | 552 | 3863 | 14 | 1.71×10^{-4} | 9.66×10^{-5} | 4.27 | 24.76 |
| W2 | 990 | 3863 | 26 | 9.07×10^{-5} | 6.35×10^{-5} | 5.32 | 58.95 |
| B1 | 733 | 3863 | 19 | 8.27×10^{-4} | 6.40×10^{-4} | 1.65 | 5.85 |
| B2 | 544 | 3863 | 14 | 3.04×10^{-4} | 2.74×10^{-4} | 2.16 | 13.35 |
| BBL | 803 | 3863 | 21 | 1.49×10^{-4} | 1.30×10^{-4} | 1.01 | 4.24 |

Log-normal fit

| Bin | mean | median | μ | [c.i.] | σ | [c.i.] |
|-----|-----------------------|-----------------------|-------|-----------------|----------|---------------|
| W1 | 1.61×10^{-4} | 1.00×10^{-4} | -9.20 | [-9.28 - -9.12] | 0.97 | [0.92 - 1.03] |
| W2 | 8.96×10^{-5} | 6.41×10^{-5} | -9.65 | [-9.70 - -9.60] | 0.81 | [0.78 - 0.85] |
| B1 | 8.34×10^{-4} | 6.49×10^{-4} | -7.33 | [-7.39 - -7.28] | 0.70 | [0.67 - 0.74] |
| B2 | 3.25×10^{-4} | 2.39×10^{-4} | -8.33 | [-8.40 - -8.27] | 0.78 | [0.73 - 0.83] |
| BBL | 1.59×10^{-4} | 1.17×10^{-4} | -9.04 | [-9.09 - -8.99] | 0.77 | [0.74 - 0.81] |

Burr XII fit

| Bin | mean | median | α | [c.i.] | c | [c.i.] | k | [c.i.] |
|-----|-----------------------|-----------------------|-----------------------|---------------------------------|------|---------------|-------|-----------------|
| W1 | 1.95×10^{-4} | 9.52×10^{-5} | 7.52×10^{-5} | [6.15 - 9.19×10^{-5}] | 2.13 | [1.86 - 2.44] | 0.71 | [0.54 - 0.92] |
| W2 | 9.40×10^{-5} | 6.33×10^{-5} | 6.02×10^{-5} | [5.09 - 7.12×10^{-5}] | 2.24 | [2.03 - 2.48] | 0.92 | [0.72 - 1.17] |
| B1 | 8.49×10^{-4} | 6.53×10^{-4} | 6.89×10^{-4} | [5.56 - 8.53×10^{-4}] | 2.41 | [2.12 - 2.73] | 1.09 | [0.79 - 1.52] |
| B2 | 3.03×10^{-4} | 2.65×10^{-4} | 6.91×10^{-4} | [4.50 - 11.0×10^{-4}] | 1.87 | [1.69 - 2.06] | 4.50 | [2.46 - 8.20] |
| BBL | 1.49×10^{-4} | 1.32×10^{-4} | 9.05×10^{-4} | [2.08 - 39.1×10^{-4}] | 1.69 | [1.55 - 1.84] | 18.24 | [2.04 - 163.08] |

(c) Quadratic fit parameters

| | $K_\epsilon = f(S_\epsilon)$ $K = aS^2 + b$ | $K_{N^2} = f(S_{N^2})$ $K = aS^2 + b$ |
|--------------------------------|------------------------------------------------|------------------------------------------|
| Coeff. (with 95% conf. bounds) | | |
| a | 1.08 (0.85 1.31) | 1.82 (0.89 2.75) |
| b | 10.9 (-13.7 35.6) | 1.30 (-12.95 15.56) |
| Goodness of fit | | |
| SSE | 322.5 | 144.8 |
| R-square | 0.98 | 0.92 |
| Adjusted R-square | 0.98 | 0.90 |
| RMSE | 10.3 | 6.94 |

430 *3.6.0.2 Relationships between observations* To complete the statistical charac-
 431 terization, we computed the skewness S and kurtosis K , which are indicators of the sym-
 432 metry and the intermittency, respectively, of the observed variable (**Fig. 7.a**). The re-
 433 lationship between kurtosis K and skewness S of the different measured parameters was
 434 assessed by fitting a quadratic function $K = aS^2 + b$ for ϵ and N^2 (fit parameters can
 435 be found in **Tab. 1.c**). Additionally, theoretical curves for the log-normal and Gamma
 436 distributions are presented to allow for a comparison. Our statistics reproduce the same
 437 behaviour as in Lozovatsky et al. [2017]. The quadratic relationship fits well the dissipa-
 438 tion rate observations (**Fig. 7.a**, squares over the black line) whose distribution is closer
 439 to the Gamma than to the log-normal distribution. Regarding the absolute values of the
 440 high order statistics, the stratified bins B1 and B2 are less symmetric and intermittent
 441 than for the surface bins W1 and W2, with the bottom bin BBL standing in between
 442 while being closer to the latter. Median values of ϵ (**Fig. 7.b**) indicate a partition be-
 443 tween stratified and mixed layers, decreasing from $11 \times 10^{-10} \text{ W kg}^{-1}$ in the transitional
 444 period summer-to-fall (W1 in green) to $4 \times 10^{-10} \text{ W kg}^{-1}$ in winter (W2 in cyan). The
 445 strongest median values are around $13 \times 10^{-10} \text{ W kg}^{-1}$ and concern the stratified bins
 446 (B1 in blue, and B2 in red). In term of distribution, N^2 (**Fig. 7.a**) appear to be close
 447 to the log-normal distribution for the stratified bins (B1 in blue triangle, B2 in red, and
 448 BBL in gray), and differ in the mixed layers (W1 in green triangle and W2 in cyan). Its
 449 kurtosis (and skewness, not shown) clearly decreases in function of the intensity of the
 450 stratification (**Fig. 7.c**).

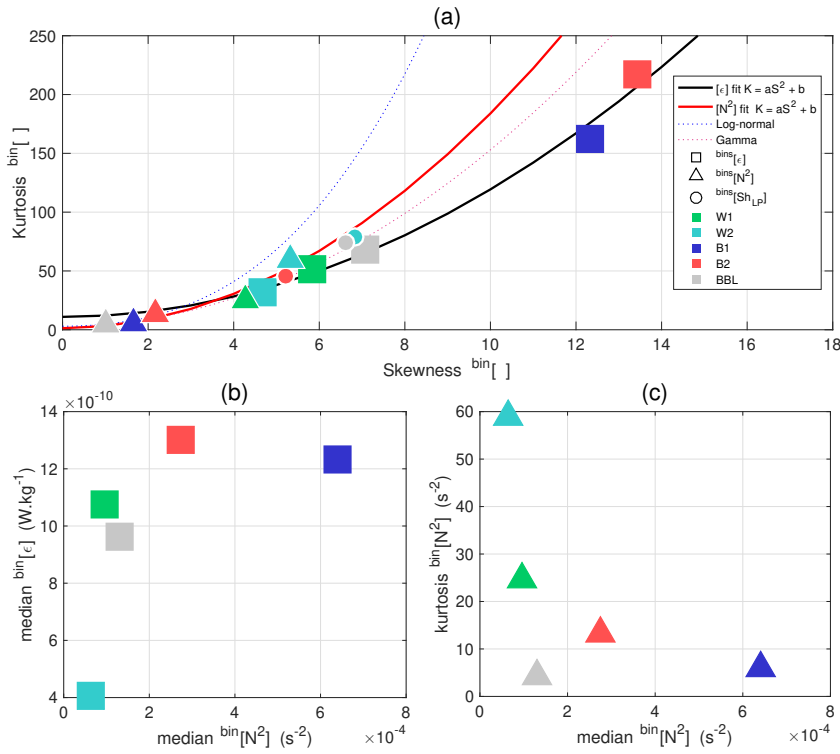


Figure 7: (a) Skewness (S) and kurtosis (K) of ϵ (squares), N^2 (triangles), and Sh_{LP} (dots), for the different temporal and vertical groups of data (colors refer to the bins on Fig. 2.c). A discussion dedicated to Sh_{LP} is given in the Appendix. Black and red plain lines indicate quadratic fits $K = aS^2 + b$ as proposed by Lozovatsky et al. [2017] and applied to ϵ and N^2 . Statistics of the parameters can be consulted in Tab. 1. Blue and red dashed lines indicates theoretical curves for log-normal and Gamma distributions. (b) Median of ϵ (W kg^{-1}) and (c) kurtosis of N^2 (s^{-2}), in function of the median of N^2 (s^{-2}).

451 **4 Discussion**

452 We used CTD and microstructure observations to depict the time evolution of the
 453 water column in the Gulf of Naples, a mid-latitude non-tidal coastal site. This data set
 454 showed a deepening of the ML starting in late summer, marked by intermittent high dis-
 455 sipation rates below the MLD. Closer to the surface, we observed short periods of en-
 456 hanced turbulence that may contribute to the deepening of the ML. We review here some
 457 mechanisms potentially relevant to explain our coastal observations, synthesised schemat-
 458 ically on **Fig. 8**.

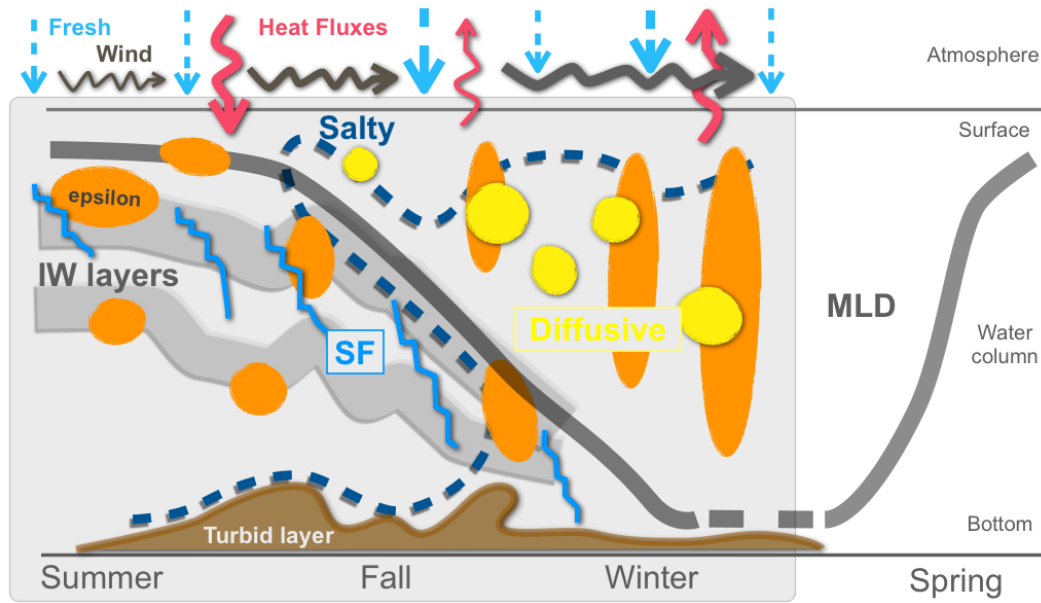


Figure 8: Schematic representation of the relevant processes identified in this study for seasonal destratification cycle, at the LTER-MC site in the Gulf Of Naples, by 75m deep, from July 2015 to February 2016. Freshwater (blue dashed arrows), wind stress (gray arrows) and buoyancy fluxes (red arrows) are represented at the surface. The salty tongue observed in the hydrology is depicted in dashed dark blue, while the turbid bottom layer is shown in brown. The MLD is schematized in thick gray. The two regions occupied by the first two baroclinic modes of internal waves (IW) are indicated by the shaded layers below the MLD. Schematic patches showing intensified turbulent kinetic energy dissipation rates are plotted in orange. Salt fingering (SF) and diffusive convection regimes are schematized by the blue stairs and the yellow circles, respectively.

459 The shallow waters of the GoN are strongly influenced by the atmospheric forcings.
 460 Positive buoyancy fluxes in summer (**Fig. 8**, pink arrow pointing down) maintain a strong
 461 stratification that light summer winds (**Fig. 8**, black curly lines) can hardly break. Storms
 462 started at the end of summer with dominating enhanced wind episodes and the first neg-
 463 ative buoyancy fluxes (**Fig. 8**, pink arrow pointing up), both contributing to a deepening
 464 of the ML. Fall and winter periods were marked by increasingly negative buoyancy
 465 fluxes and few intermittent episodes of strong wind.

466 Regarding the water column T-S properties, the close-by Sarno River, located in
 467 the northeast corner of the GoN (**Fig. 1**), is a potential source of freshwater anomalies
 468 propagating along the east side of the Gulf. This river could thus be the main source of
 469 the low salinity content of surface waters observed from July to October (**Fig. 8**, ver-
 470 tical dashed blue arrows) even if the study of Cianelli et al. [2012] showed that this in-

471 fluence should be constrained to the eastern part of the GoN. Satellite observations in
 472 recent studies of the regional circulations suggest an indirect influence of the Volturno
 473 river located in the Gulf of Gaeta (to the northwest and out of the GoN), whose nutrient-
 474 rich waters may reach the GoN through mesoscale and submesoscale features forced by
 475 the westerly wind events (Iermano et al. [2012]). A local pooling effect could exist in sum-
 476 mer, with freshwater trapped at the coast by the daily oscillation of breeze winds (Cianelli
 477 et al. [2017]). The nearby Tyrrhenian sea instead acts as a source for the salty waters
 478 that were observed at depth from July to October, and over the whole water column later
 479 in the year (**Fig. 8**, dashed dark blue line). These salty intrusions into the GoN are pos-
 480 sibly at the origin of the salt-fingers patterns we identified and related to the the fine
 481 density steps we observed in our data set (**Fig. 8**, blue stairs). These steps-like features
 482 are present the coastal area, but manifesting on smaller scales than the typical Tyrrhe-
 483 nian stairs (Durante et al. [2019]). There, they may be related to interleaving events (Rud-
 484 dick & Richards [2003]), and their vertical structure in layers of 0.3 to 3 m-thick is co-
 485 herent with the case of a strong stratification and intermittent and weak mixing (Lin-
 486 den [1976], Turner [1983]). Double diffusive processes could be at the origin of a net trans-
 487 fer of mass toward the bottom layers and they could play an important role for the ver-
 488 tical transfer of nutrients available for biological species (Ruddick & Turner [1979]). The
 489 impact of salt-fingering on the duration of the stratified period remains to be quantified,
 490 even in such coastal areas where they are usually assumed to be insignificant. During
 491 the fall season, the unstable vertical salinity gradients progressively weakened, making
 492 subsurface layers more prone to diffusive convection (**Fig. 8**, yellow circles).

493 These upper layer processes that contribute to the ML deepening found their en-
 494 ergy source in the atmospheric forcings. Below the ML, the energy for sustaining the mix-
 495 ing is possibly brought by internal wave activity as the sheared layers suggest (**Fig. 8**,
 496 gray shaded layers). Measurements of the large scale shear are planned for future cruises
 497 to try to quantify this energy transfer.

498 Next, we consider various mechanisms that may be relevant to explain the seasonal
 499 succession of mixing events. Due to the specific vertical structure observed in the GoN
 500 during the stratified period, with warm salty waters overlying cooler and fresher waters,
 501 salt-fingering can be active. This provides a particular hydrological context for the gen-
 502 eration, propagation and mixing of internal waves (Inoue et al. [2007], Maurer & Lin-
 503 den [2014]). Locally, internal waves could also be generated by wind-driven rapid deep-
 504 ening, supported also by Langmuir motions forced by the surface wave field (Polton et
 505 al. [2008]). It is noteworthy that we did not sample during storms, which also act as lo-
 506 cal sources of internal waves. The proximity of the coast could play an important role
 507 in forcing internal waves, following the recent study of Kelly [2019]. They found that a
 508 coastal reflection of wind-driven inertial oscillations in the ML could generate offshore
 509 propagating near-inertial waves, associated to an intensified shear in the region below
 510 the ML (e.g. their Fig. 8). Indeed, the GoN coast is only 2 km away from the sampling
 511 site and we observed an intensification of shear events during the fall season, characterised
 512 by intense storminess and intermediate MLDs. Therefore, this specific mechanism could
 513 contribute to create these vertical shear events we observed in correspondence of the main
 514 baroclinic modes. In turn, this could contribute to the destratification of the water col-
 515 umn during the transition to the winter state. The morphology of the GoN could be a
 516 source of internal waves generation too. Internal waves generated by current-topography
 517 interaction can radiate from the shelf to the coast with strong imprint on the first two
 518 baroclinic modes (Xie & Li [2019]). The existence of steep canyons in the GoN, and no-
 519 tably the Dohrn Canyon at south, provides a topographical configuration that could act
 520 as source for the generation of on-shore propagating waves. A current-topography in-
 521 teraction could be sustained also by the various bathymetrical features close to the coast
 522 (the Banco della Montagna, the Ammontatura channel and the Mt. Somma-Vesuvius
 523 complex on Fig. 1 in Passaro et al. [2016], located south, southwest and northeast from

the LTER-MC sampling point). Finally, a recurrent transition of Kelvin coastal trapped waves over the area has been proposed in the numerical study by de Ruggiero et al. [2018].

The oceanic response to climate change involves several processes, with various degrees of complexity. To reach a full predictive capability it is important to characterise their respective roles and the associated temporal and spatial variability. The analysis of the distribution of ϵ through the different periods represents a step toward a statistical characterization of ϵ , as investigated by the recent studies on the distribution in the interior ocean (Lozovatsky et al. [2017], Buckingham et al. [2019]). We showed that dissipation rates in the ML follows a Burr XII distribution instead of a lognormal. This result requires further study since a lognormal behaviour is considered as ubiquitous for such intermittent features (Pearson & Fox-Kemper [2018]). The respective roles of temporal intermittency and spatial heterogeneity remain to be determined. Finally, it is to note that the use of a small research vessel did not allow for sampling in rough weather and, therefore, the temporal intermittency is here presumably highly underestimated. This points to the need of microstructure observations that are designed to fully cover the spectrum of space and time scales (Pearson & Fox-Kemper [2018]). These specific challenges have to be met in the next future (Benway et al. [2019]) along with long-term observations to constrain the current climate change. Effort could include the deployment of microstructure devices mounted on moorings and wirewalker systems (Pinkel et al. [2011]), or to design and deploy dedicated drifters that regularly sample the water column as it is the case for the Argo floats (Roemmich et al. [2019]). In addition to following well-known probability distributions, we observed a quadratic relation between kurtosis and skewness in the statistics of ϵ , as it has been shown and discussed in the studies of Schopflicher & Sullivan [2005] and Lozovatsky et al. [2017]. This remarkable fit is quite universal since it does not depend upon the specificity of the physics's laws. It fits quite well also the low pass component of the microstructure shears, that was not used for estimating ϵ . In addition, the low pass shear events have a layer-averaged intensity that is linearly increasing with N^2 . Statistics on the degree of intermittency, instead, are specific to the environmental conditions, that is, they are different for the ML and the interior.

Our microstructure survey was part of the long term monitoring of the coastal area of the GoN, by the Marechiarra project started in 1984 and running until now. It provided an unique view, from July 2015 to February 2016, on the seasonal cycle of the stratification and mixing in the GoN. In the companion study in preparation, that investigated CTD and forcing data over 2001-2020, we derived the mean seasonal cycles of the water column structure. When compared to the bi-decadal mean cycles it is found that the water column in 2015 was fresher and accumulated relatively less heat, the late summer period being marked by significant rain event and moderate winds. In this study we observed that the long term thermal components (water column heat content, surface temperature) at the sampling site of the GoN did not exhibit increasing decadal trends as those observed over the Mediterranean basin (Pisano et al. [2020]), in contrary of the freshwater components reflecting the redistribution of precipitation at larger scale. So, in addition to a regional warming (e.g., heatwaves), the question of both the influence of larger scale actors (atmospheric systems changes) and intermittent events is to be considered (Baldi et al. [2006])). This promotes the efforts of long-term observations over these coastal areas to better understand the various processes and distinguish among them which ones (if not all) are more sensitive to future climate change. The complexity of mechanisms at finescales whose interplay produce convection, shear, mixing, leading to the ML deepening, can be significantly modulated by long-term heat, freshwater and wind changes (Somavilla et al. [2017]). In conclusion, we suggest that sites such as the GoN, a shelf region in a non-tidal area, are of interest for discriminating between processes less energetic than tides, as internal waves or even double-diffusion, beyond the global warming and the consequent increase of the stratification (Woodson [2018], Guancheng et al. [2020]).

578 Appendix A Low frequency signals in the microstructure shears data

579 This section is motivated by the repeated observation of a low-frequency signal in
 580 our microstructure shear data, while the instrument’s fall speed remained constant. This
 581 signal was observed within stratified layers, at the MLD and below the MLD, depicting
 582 vertical patterns during our survey (**Fig. A1**). We propose here a first attempt to separate
 583 parts of the signal that may be due to strong thermal gradients (pyro-effect, as discussed
 584 after), and other ones possibly due to other noise sources, or real energetic motions.
 585 The shear probes are sensitive to velocity fluctuations at frequencies greater than
 586 0.1 Hz, but the signals are often high-pass filtered at higher frequencies (~ 0.4 Hz) before
 587 computing the spectra and the dissipation rate. Here we intended to carefully use the
 588 low frequency part of shear signals since no other sources of velocity shear were available.
 589 However, it is most likely that the low-frequency response in the micro-structure
 590 shear data is due to passing through strong thermal gradients, an effect known as the
 591 pyro-electric effect, which cannot be interpreted as a physical shear signal (see below).
 592 Despite this, an analysis of the low frequency signal still shows some interesting patterns
 593 that are worth presenting.

594 For the analysis, we defined low-passed shear energy estimates $Sh_{LP}^{1,2}$ from shear
 595 1 and 2, calculated by low-pass filtering the despiked shears at 0.1 Hz, as

$$596 Sh_{LP}^{1,2} = \langle (du/dz)^2 \rangle_{LP}^{0.1Hz}, \quad \langle (dv/dz)^2 \rangle_{LP}^{0.1Hz}.$$

597 In our dataset, structures linked to this low-frequency signal showed vertical scales
 598 of around 3 m. We show on **Fig. A1** time filtered quantities at 0.1 Hz, that are equivalent
 599 to a spatial filtering over these length scales. We note that spatial filtering has the
 600 advantage to avoid numerical negative values (e.g. if used to estimate a proper energy
 601 content).

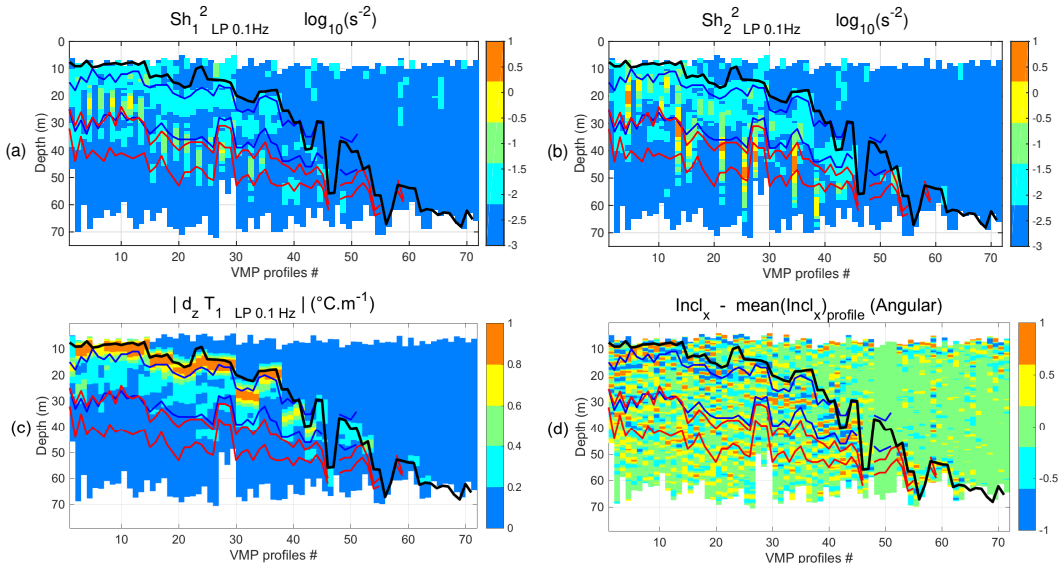


Figure A1: Square value of the microstructure shears 1 (a) and 2 (b) (i.e. du/dz and dv/dz , respectively) low pass filtered at 0.1 Hz (s^{-2}). We plotted the absolute values due to numerical negative values created by the filtering after the square operator. Profiles examples are shown on supplementary Fig. S3. (c) Microstructure gradients dT/dz ($^{\circ}m^{-1}$) low-passed filtered at 0.1 Hz, and plotted in absolute value, showing subsurface layers concerned by strong vertical thermal gradients. These are mainly located between the base of the MLD and the upper limit of the envelope of the baroclinic mode B1. (d) Anomaly to the mean value of the roll inclination of the VMP-250 (angular $^{\circ}$ relative to the x-axis).

Pyro-electric effect

Shear probes occasionally respond to large changes in temperature with the sudden release (or absorption) of electric charge that generates a large amplitude signal, even when no strain is applied to the ceramic beam (Lueck et al. [2002]). This effect is referred to as the pyro-electric effect (Muralt [2005]) and can occur when probes pass through large temperature gradients. To minimize this effect, the piezo-ceramic element in the shear probe is insulated from the environment by a layer of epoxy and the electronics are designed to high-pass filter the signal at 0.1 Hz (Rockland's Technical Note 005). Despite these precautions in the sensor design, some shear probes may still respond to sharp changes in temperature. In this study, the response was somewhat unpredictable and probe-dependent.

This signal was present in the subsurface shear data, when the profiler passed through the strong seasonal vertical gradients of temperature, leading to contamination of the shear signal at low frequencies between 0.1 and 1 Hz. The amplitude of the temperature gradient at the base of the MLD was approximately 1°m^{-1} in summer, to 0.3°m^{-1} during the transition from fall to winter (**Fig. A1.c**). The two shear probes responded differently when crossing the same vertical temperature gradient: shear 1 appeared to be less sensitive than shear 2 in general, with values of 3 times smaller in average, and less concerned by surface gradients. In general the resulting low-frequency signal was present up to nearly 1 Hz. To avoid temperature contamination of dissipation rate estimates in the rest of our study, we applied a high-pass filtering with a cut-off frequency of 1.5 Hz on the despiked micro-structure shears before using them to compute the spectra and estimate ϵ (see Methods). We considered the spare probe shear 2 suitable for estimating ϵ from its high-frequency content, but its low-frequency signal is probably contaminated by pyro-effect on subsurface, and intensified noisy response in the deep layers.

Low-frequency content below the strong surface gradients

As visible on (**Fig. A1**), a repetitive low frequency signal was intermittently present too in the deep layers at a 20m-distance below the MLD, both on shear 1 and 2. In contrary of the surface, these layers are concerned by moderated thermal gradients, and the shear response to this vertical structure should be presumably be free from pyro-electric contamination. We observe that this signal is distributed through the vertical envelope of the baroclinic modes of internal waves (as we defined it), and is frequently associated with small and slow oscillations of $\pm 2^\circ$ of the instrument roll (**Fig. A1.d**), even no specific noise contamination was visible through the accelerometers. Moreover, it appears to be co-located with other independent physical parameters, as we show it on the physical examples taken from the distinct CTD cast and the fluorometer sensor on supplementary Fig. S3. Out of affirming that we identified here a physical signal in the micro-structure shear, we decided to carry apart this low frequency shear signal through our analysis, to show its statistics, as we separated it properly from the high-passed shear used to infer ϵ . We selected only the estimation based on shear 1. To avoid numerical negative values and estimate a proper energy content, we filtered spatially instead of temporally and propose $Sh_{LP} = \langle (du/dz)^2 \rangle_{LP}^m$.

Possible link between Sh_{LP} and ϵ

The stratified layers possibly containing internal wave activity were remarkably co-located with the low-passed energy component Sh_{LP} events, the latter potentially being a proxy of energetic motions, even though its values are challenging to interpret. In particular, two regions exhibit enhanced low pass shear levels (**Fig. A2.a**). The first one is associated with the baroclinic mode region B1: a clear intensification is located below the MLD and follows its deepening from July to early October while another maximum is located around 20-30 m in July and early August. The second one is associated

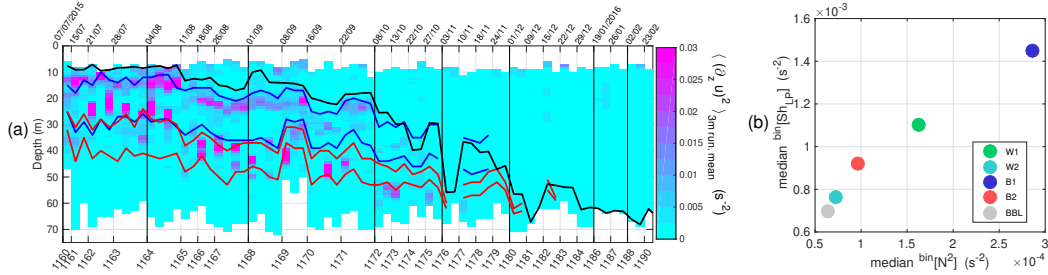


Figure A2: (a) Low pass shear energy Sh_{LP} i.e. $\langle (\partial_z u)^2 \rangle_{LP}^{3m}$ (s^{-2}), $MLD_{\theta_0}^{0.4^\circ C}$ (thick black line), region of maximum energy of baroclinic mode 1 (between blue lines) and mode 2 (between red lines). The VMP profiles are plotted sequentially along the x-axis, where the MC casts references are indicated (from one to four VMP profiles by cast). Sampling dates are given on the panel top. (b) Median of Sh_{LP} (s^{-2}) in function of the median of N^2 (s^{-2}).

652 with B2 and it is clearly visible during August and September while having less intense
 653 imprint in July and October. Elsewhere, the low pass shear is weak whenever the stratification is weak (e.g., ML and BBL). Pdfs are shown in the supplementary information
 654 (Fig. S4). Although Sh_{LP} and ϵ are estimated over totally independent wavenumber ranges,
 655 their kurtosis-skewness relationship follows the same quadratic fit out of the log-normality
 656 (Fig. 7.a, dots and squares). In addition, Sh_{LP} shows a remarkable linearity as a function of the stratification intensity (Fig. A2.b), while ϵ does not show such a linear relationship with the stratification (Fig. 7.a). The Sh_{LP} estimate presented here is not
 657 conventional and its interpretation would require a thoughtful validation via a comparison with Acoustic Doppler Current Profiler (ADCP) observations. While to be considered with great caution, we documented in Fig. S5 the distribution of ϵ in function of N^2 and Sh_{LP} as proxy of the shear (Gill [1982], Monin & Yaglom [2007]). Interestingly, it shows higher ϵ values in correspondence with a weaker stratification and larger shear values. The dependence from the stratification intensity is lost in the ML (W1 and W2), while a modulation by N is suggested in the stratified layers B1, B2 and BBL, following the observations of Vladoiu et al. [2018] that tested a wave-wave parameterization for ϵ based on MacKinnon & Gregg [2003].
 658
 659
 660
 661
 662
 663
 664
 665
 666
 667
 668

Acknowledgments

669 Data sets for this research are available under netcdf format on <https://github.com/nerea-observatory/ltermc-microstructure>. We would like to thank the LTER-MC team that includes, besides the main authors: D. d’Alelio, C. Balestra, M. Cannavaciuolo, R. Casotti, I. Di Capua, F. Margiotta, M. G. Mazzocchi, M. Montresor, A. Passarelli, I. Percopo, M. Ribera d’Alcalà, M. Saggiomo, V. Saggiomo, D. Sarno, F. Tramontano, G. Zazo, A. Zingone, all based at Stazione Zoologica Anton Dohrn of Naples. Special thanks must be given to the commandants and crews of the R/V Vettoria. The research program LTER-MC is supported by the Stazione Zoologica Anton Dohrn.
 670
 671
 672
 673
 674
 675
 676
 677

References

678
 679 Albanese, S., Iavazzo, P., Adamo, P., Lima, A., & De Vivo, B. (2012, 09). Assessment of the environmental conditions of the sarno river basin (south italy): A stream sediment approach. *Environmental Geochemistry and Health*, 35. doi: 10.1007/s10653-012-9483-x
 680
 681
 682
 683 Baldi, M., Dalu, G., Maracchi, G., Pasqui, M., & Cesarone, F. (2006, 09). Heat

- 684 waves in the mediterranean: A local feature or a larger-scale effect? *International*
685 *Journal of Climatology*, *26*, 1477–1487. doi: 10.1002/joc.1389
- 686 Barton, A., Ward, B., Williams, R., & Follows, M. (2014, 04). The impact of fine-
687 scale turbulence on phytoplankton community structure. *Limnology and Oceanog-*
688 *raphy: Fluids and Environments*, *4*. doi: 10.1215/21573689-2651533
- 689 Benway, H. M., Lorenzoni, L., White, A. E., Fiedler, B., Levine, N. M., Nicholson,
690 D. P., . . . Letelier, R. M. (2019). Ocean time series observations of changing
691 marine ecosystems: An era of integration, synthesis, and societal applications.
692 *Frontiers in Marine Science*, *6*, 393. doi: 10.3389/fmars.2019.00393
- 693 Brainerd, K. E., & Gregg, M. C. (1995). Surface mixed and mixing layer depths.
694 *Deep-Sea Research I*, *42*, 1521–1543.
- 695 Brody, S. R., , & Lozier, M. S. (2014). Changes in dominant mixing length scales
696 as a driver of subpolar phytoplankton bloom initiation in the north atlantic. *Geo-*
697 *physical Research Letter*, *41* (9), 3197–3203.
- 698 Buckingham, C. E., Lucas, N. S., Belcher, S. E., Rippeth, T. P., Grant, A. L. M., ,
699 & Lesommer, J. (2019). The contribution of surface and submesoscale processes to
700 turbulence in the open ocean surfaceboundary layer. *Journal of Advances in Mod-*
701 *eling Earth Systems*, *11*, 4066–4099. doi: <https://doi.org/10.1029/2019MS001801>
- 702 (C3S), C. C. C. S. (2017). Era5: Fifth generation of ecmwf atmospheric reanaly-
703 ses of the global climate. *Copernicus Climate Change Service Climate Data Store*
704 *(CDS)*, date of access. doi: <https://cds.climate.copernicus.eu/cdsapp#!/home>
- 705 Cianelli, D., D’Alelio, D., Uttieri, M., Sarno, D., Zingone, A., Zambianchi, E., &
706 Ribera d’Alcala, M. (2017, 12). Disentangling physical and biological drivers
707 of phytoplankton dynamics in a coastal system. *Scientific Reports*, *7*. doi:
708 10.1038/s41598-017-15880-x
- 709 Cianelli, D., Uttieri, M., Buonocore, B., Falco, P., Zambardino, G., & Zambianchi,
710 E. (2012, 08). Dynamics of a very special mediterranean coastal area: the gulf of
711 naples. *Mediterranean Ecosystems: Dynamics, Management and Conservation*,
712 129–150.
- 713 de Boyer Montégut, C., Madec, G., Fischer, A. S., Lazar, A., & Iudicone, D. (2004,
714 01). Mixed layer depth over the global ocean: An examination of profile data and
715 profile-based climatology. *Journal of Geophysical Research*, *109*, C12003. doi: 10
716 .1029/2004JC002378
- 717 de Ruggiero, P., Ernesto, N., Iacono, R., Pierini, S., & Spezie, G. (2018, 09). A baro-
718 clinic coastal trapped wave event in the gulf of naples (tyrrhenian sea). *Ocean Dy-*
719 *namics*. doi: 10.1007/s10236-018-1221-1
- 720 Durante, S., Schroeder, K., Mazzei, L., Pierini, S., Borghini, M., & Sparnocchia, S.
721 (2019, 01). Permanent thermohaline staircases in the tyrrhenian sea. *Geophysical*
722 *Research Letters*. doi: 10.1029/2018GL081747
- 723 Ferrari, R., & Wunsch, C. (2009). Ocean circulation kinetic energy: Reservoirs,
724 sources, and sinks. *Annual Review of Fluid Mechanics*, *41*, 253–282.
- 725 Garrett, C., Keeley, J., & Greenberg, D. (1978, 12). Tidal mixing versus thermal
726 stratification in the bay of fundy and gulf of maine. *Atmosphere-Ocean*, *16*, 403–
727 423. doi: 10.1080/07055900.1978.9649046
- 728 GEBCO, C. G. (2020). *Gebco 2020 grid*. Retrieved from <https://www.gebco.net>
729 doi: 10.5285/a29c5465-b138-234d-e053-6c86abc040b9
- 730 Gill, A. (1982, 01). Atmosphere-ocean dynamics. In (Vol. 30, p. 662).
- 731 Goodman, L., Levine, E. R., , & Lueck, R. G. (2006). On measuring the terms
732 of the turbulent kinetic energy budget from an auv. *Journal of Atmospheric and*
733 *Oceanic Technology*, *23*, 977–990.
- 734 Guancheng, I., Cheng, L., Zhu, J., Trenberth, K., Mann, M., & Abraham, J. (2020,
735 09). Increasing ocean stratification over the past half-century. *Nature Climate*
736 *Change*, 1–8. doi: 10.1038/s41558-020-00918-2
- 737 Hegerl, G. C., Black, E., Allan, R. P., Ingram, W. J., Polson, D., Trenberth, K. E.,

- 738 ... Zhang, X. (2015). Challenges in quantifying changes in the global water cycle.
739 *Bulletin of the American Meteorological Society*, *96*(7), 1097–1115.
- 740 Iermano, I., Liguori, G., Iudicone, D., Buongiorno Nardelli, B., Colella, S., Zingone,
741 A., ... Ribera d'Alcala, M. (2012). Dynamics of short-living filaments and their
742 relationship with intense rainfall events and river flows. *Progress in Oceanography*,
743 *106*, 118–137. doi: 10.1016/j.pocean.2012.08.003
- 744 Inoue, R., Yamazaki, H., Wolk, F., Kono, T., & Yoshida, J. (2007, 03). An estima-
745 tion of buoyancy flux for a mixture of turbulence and double diffusion. *Journal of*
746 *Physical Oceanography*, *37*. doi: 10.1175/JPO2996.1
- 747 Johnston, T., & Rudnick, D. (2009, 03). Observations of the transition layer. *Jour-
748 nal of Physical Oceanography*, *39*. doi: 10.1175/2008JPO3824.1
- 749 Kelly, S. (2019, 09). Coastally generated near-inertial waves. *Journal of Physical*
750 *Oceanography*, *49*. doi: 10.1175/JPO-D-18-0148.1
- 751 Kiørboe, T., & Mackenzie, B. (1995, 12). Turbulence-enhanced prey encounter rates
752 in larval fish: Effects of spatial scale, larval behaviour and size. *Journal of Plank-
753 ton Research*, *17*, 2319–2331. doi: 10.1093/plankt/17.12.2319
- 754 Koseki, S., Mooney, P., Cabos Narvaez, W. D., Gaertner, m., de la Vara, A., & Ale-
755 man, J. (2020, 07). Modelling a tropical-like cyclone in the mediterranean sea
756 under present and warmer climate.
757 doi: 10.5194/nhess-2020-187
- 758 Large, W., & Pond, S. (1981, 01). Open ocean momentum flux measurement in
759 moderate to strong winds. *Journal of Physical Oceanography*, *11*, 336–342.
- 760 Linden, P. (1976, 10). The formation and destruction of fine-structure by double-
761 diffusive processes. *Deep Sea Research and Oceanographic Abstracts*, *23*, 895–908.
762 doi: 10.1016/0011-7471(76)90820-2
- 763 Lozovatsky, I., H.J.S., F., J., P.-M., Liu, Z., Lee, J. H., & Jinadasa, S. (2017, 08).
764 Probability distribution of turbulent kinetic energy dissipation rate in ocean:
765 Observations and approximations. *Journal of Geophysical Research*, *122*. doi:
766 10.1002/2017jc013076
- 767 Lueck, R. (2016). Rsi technical note 028 : Calculating the rate of dissipation of tur-
768 bulent kinetic energy. *Rockland Scientific International Inc.*
- 769 Lueck, R., Wolk, F., & Yamazaki, H. (2002, 02). Oceanic velocity microstructure
770 measurements in the 20th century. *Journal of Physical Oceanography*, *58*, 153–
771 174. doi: 10.1023/A:1015837020019
- 772 MacKinnon, J., & Gregg, M. (2003, 07). Mixing on the late-summer new england
773 shelf—solibores, shear, and stratification. *Journal of Physical Oceanography*, *33*,
774 1476–1492. doi: 10.1175/1520-0485(2003)033<1476:MOTLNE>2.0.CO;2
- 775 Mackinnon, J. A., & Gregg, M. C. (2005). Near-inertial waves on the new england
776 shelf: The role of evolving stratification, turbulent dissipation, and bottom drag.
777 *Journal of Physical Oceanography*, *35*, 2408–2424.
- 778 Mann, K. H., & Lazier, J. R. N. (1996). *Dynamics of marine ecosystems*.
- 779 Maurer, B., & Linden, P. (2014, 08). Intrusion-generated waves in a linearly strati-
780 fied fluid. *Journal of Fluid Mechanics*, *752*, 282–295. doi: 10.1017/jfm.2014.316
- 781 McDougall, T., & Barker, P. (2011). Getting started with teos-10 and the gibbs sea-
782 water (gsw) oceanographic toolbox. *SCOR/IAPSO WG*, *127*, 1–28.
- 783 Monin, A., & Yaglom, A. (2007). *Statistical fluid mechanics, volume 1: Mechanics of*
784 *turbulence*.
- 785 Muralt, P. (2005). Pyroelectricity. In F. Bassani, G. L. Liedl, & P. Wyder (Eds.),
786 *Encyclopedia of condensed matter physics* (pp. 441–448). Oxford: Elsevier. doi: 10
787 .1016/B0-12-369401-9/00434-4
- 788 Nuttall, A. H. (1971). Spectral estimation by means of overlapped fast fourier trans-
789 form processing of windowed data. *NUSC Tech. Rep. No. 4169*. doi: https://apps
790 .dtic.mil/sti/pdfs/AD0739315.pdf

- 791 Obukhov, A. (n.d.). Turbulentnost'v temperaturnojneodnorodnoj atmosfere ("turbu-
792 lence in an atmosphere with a non-uniform temperature"). *Tr. Inst. Teor. Geofiz.*
793 *Akad. Nauk. SSSR.*, 1, 95–115.
- 794 Obukhov, A. (1971, 01). Turbulence in an atmosphere with non-uniform tempera-
795 ture. *Boundary-Layer Meteorology*, 2, 7–29. doi: 10.1007/BF00718085
- 796 Osborn, T. (1998, 01). Finestructure, microstructure, and thin layers. *Oceanography*,
797 11. doi: 10.5670/oceanog.1998.13
- 798 Passaro, S., Tamburrino, S., Vallefucio, M., Gherardi, S., Sacchi, M., & Guido, V.
799 (2016, 06). High-resolution morpho-bathymetry of the gulf of naples, eastern
800 tyrrhenian sea. *Journal of Maps*, 1–8. doi: 10.1080/17445647.2016.1191385
- 801 Pastor, F., Valiente, J. A., , & Palau, J. L. (2018). Sea surface temperature in the
802 mediterranean: Trends and spatial patterns (1982–2016). *Pure and Applied Geo-*
803 *physics*, 175, 4017–4029. doi: https://doi.org/10.1007/s00024-017-1739-z
- 804 Pearson, B., & Fox-Kemper, B. (2018, 02). Log-normal turbulence dissipation in
805 global ocean models. *Physical Review Letters*, 120. doi: 10.1103/PhysRevLett.120
806 .094501
- 807 Pingree, R., Holligan, P., Mardell, G., & Head, R. (1976, 11). The influence of phys-
808 ical stability on spring, summer and autumn phytoplankton blooms in the celtic
809 sea. *Journal of the Marine Biological Association of the United Kingdom*, 56,
810 845–873. doi: 10.1017/S0025315400020919
- 811 Pinkel, R., Goldin, M., Smith, J., Sun, O., Aja, A., Bui, M., & Hughen, T. (2011,
812 03). The wirewalker: A vertically profiling instrument carrier powered by ocean
813 waves. *Journal of Atmospheric and Oceanic Technology*, 28, 426–435. doi:
814 10.1175/2010JTECHO805.1
- 815 Pisano, A., Marullo, S., Artale, V., Falcini, F., Yang, C., Leonelli, F., . . . Buon-
816 giorno Nardelli, B. (2020, 01). New evidence of mediterranean climate change and
817 variability from sea surface temperature observations. *Remote Sensing*, 12. doi:
818 10.3390/rs12010132
- 819 Polton, J., Smith, J., Mackinnon, J., & Tejada-Martínez, A. (2008, 07). Rapid
820 generation of high-frequency internal waves beneath a wind and wave forced
821 oceanic surface mixed layer. *Geophysical Research Letters*, 35. doi: 10.1029/
822 2008GL033856
- 823 Prairie, J., Sutherland, K., Nickols, K., & Kaltenberg, A. (2012, 04). Biophysical
824 interactions in the plankton: A cross-scale review. *Limnology and Oceanography:*
825 *Fluids and Environments*, 2. doi: 10.1215/21573689-1964713
- 826 Ribera d'Alcala, M., Conversano, F., Corato, F., Licandro, P., Mangoni, O., Marino,
827 D., . . . Zingone, A. (2004, 04). Seasonal patterns in plankton communities in
828 pluriannual time series at a coastal mediterranean site (gulf of naples): An at-
829 tempt to discern recurrences and trends. *Scientia Marina*, 68, 65–83.
- 830 Roemmich, D., Alford, M., Claustre, H., Johnson, K., King, B., Moum, J., . . . Ya-
831 suda, I. (2019, 08). On the future of argo: A global, full-depth, multi-disciplinary
832 array. *Frontiers in Marine Science*, 6. doi: 10.3389/fmars.2019.00439
- 833 Ruddick, B. (1983, 10). A practical indicator of the stability of the water column to
834 double-diffusive activity. *Deep Sea Research Part A. Oceanographic Research Pa-*
835 *pers*, 30, 1105–1107. doi: 10.1016/0198-0149(83)90063-8
- 836 Ruddick, B., Anis, A., & Thompson, K. (2000, 11). Maximum likelihood spectral
837 fitting: The batchelor spectrum. *Journal of Atmospheric and Oceanic Technology*,
838 17, 1541–1555. doi: 10.1175/1520-0426(2000)017<1541:MLSFTB>2.0.CO;2
- 839 Ruddick, B., & Richards, K. (2003, 03). Oceanic thermohaline intrusions: Observa-
840 tions. *Progress In Oceanography*, 56, 499–527. doi: 10.1016/S0079-6611(03)00028
841 -4
- 842 Ruddick, B., & Turner, J. (1979, 08). The vertical length scale of double-diffusive in-
843 trusions. *Deep Sea Research Part A. Oceanographic Research Papers*, 26, 903–913.
844 doi: 10.1016/0198-0149(79)90104-3

- 845 Schopflocher, T., & Sullivan, P. (2005, 06). The relationship between skewness and
 846 kurtosis of a diffusing scalar. *Boundary-Layer Meteorology*, *115*, 341–358. doi: 10
 847 .1007/s10546-004-5642-7
- 848 Shang, X., Qi, Y., Chen, G., Liang, C., Lueck, R., Prairie, B., & Li, H. (2016, 10).
 849 An expendable microstructure profiler for deep ocean measurements. *Journal of*
 850 *Atmospheric and Oceanic Technology*, *34*. doi: 10.1175/JTECH-D-16-0083.1
- 851 Skliris, N., Marsh, R., Josey, S. A., Good, S. A., Liu, C., & Allan, R. P. (2014).
 852 Salinity changes in the world ocean since 1950 in relation to changing sur-
 853 face freshwater fluxes. *Climate Dynamics*, *43*(3-4), 709–736. doi: 10.1007/
 854 s00382-014-2131-7
- 855 Somavilla, R., Gonzalez-Pola, C., , & Fernandez-Diaz, J. (2017). The warmer the
 856 ocean surface, the shallower the mixed layer. how much of this is true? *Journal of*
 857 *Geophysical Research*, *122*(9), 7698–7716. doi: 10.1002/2017JC013125
- 858 Sverdrup, H. (1953, 01). On conditions for the vernal blooming of phytoplankton. *J.*
 859 *Cons. int. Explor. Mer*, *18*, 287–295. doi: 10.1093/icesjms/18.3.287
- 860 Thorpe, S. A. (2005). *The turbulent ocean*. Cambridge University Press.
- 861 Turner, J. (1967, 10). Salt fingers across a density interface. *Deep Sea Research and*
 862 *Oceanographic Abstracts*, *14*, 599-611. doi: 10.1016/0011-7471(67)90066-6
- 863 Turner, J. (1973, 01). Buoyancy effects in fluids.
 864 doi: 10.1017/CBO9780511608827
- 865 Turner, J. (1983). Oceanic fine and microstructure. *Brewer P.G. (eds) Oceanogra-*
 866 *phy*.
- 867 Vladoiu, A., Bouruet-Aubertot, P., Cuypers, Y., Ferron, B., Schroeder, K., Borghini,
 868 M., ... Ben Ismail, S. (2018, 05). Turbulence in the sicily channel from mi-
 869 crostructure measurements. *Deep Sea Research Part I: Oceanographic Research*
 870 *Papers*. doi: 10.1016/j.dsr.2018.05.006
- 871 Volosciuk, C., Maraun, D., Semenov, V. A., Tilinina, N., Gulev, S. K., , & Latif,
 872 M. (2016). Rising mediterranean sea surface temperatures amplify extreme
 873 summer precipitation in central europe. *Scientific Reports*, *6*(32450). doi:
 874 10.1038/srep32450
- 875 Wheeler, J. D., Secchi, E., Rusconi, R., , & Stocker, R. (2019). Not just going with
 876 the flow: The effects of fluid flow on bacteria and plankton. *The Annual Review of*
 877 *Cell and Developmental Biology*.
- 878 Wihsgotta, J. U., Sharples, J., Hopkins, J. E., Woodward, E. M. S., Huld, T.,
 879 Greenwood, N., ... Sivyer, D. B. (2019). Observations of vertical mixing in
 880 autumn and its effect on the autumn phytoplankton bloom. *Progress in Oceanog-*
 881 *raphy*, *177*.
- 882 Wolk, F., Yamazaki, H., Seuront, L., & Lueck, R. (2002, 05). A new free-fall profiler
 883 for measuring biophysical microstructure. *Journal of Atmospheric and Oceanic*
 884 *Technology*, *19*. doi: 10.1175/1520-0426(2002)019<0780:ANFFPF>2.0.CO;2
- 885 Woodson, C. (2018, 01). The fate and impact of internal waves in nearshore ecosys-
 886 tems. *Annual Review of Marine Science*, *10*. doi: 10.1146/annurev-marine-121916
 887 -063619
- 888 Wunsch, C., & Ferrari, R. (2004). Vertical mixing, energy, and the general circula-
 889 tion of the oceans. *Annual Review of Fluid Mechanics*, *36*, 281–314.
- 890 Xie, X., & Li, M. (2019, 04). Generation of internal lee waves by lateral circulation
 891 in a coastal plain estuary. *Journal of Physical Oceanography*, *49*. doi: 10.1175/
 892 JPO-D-18-0142.1
- 893 Zhang, H.-M., & Talley, L. (1998, 10). Heat and buoyancy budgets and mix-
 894 ing rates in the upper thermocline of the indian and global oceans. *Journal of*
 895 *Physical Oceanography*, *28*, 1961–1978. doi: 10.1175/1520-0485(1998)028<1961:
 896 HABBAM>2.0.CO;2
- 897 Zhang, W., Villarini, G., Scoccimarro, E., & Napolitano, F. (2020, 05). Examining
 898 the precipitation associated with medicanes in the high-resolution era-5 reanalysis

899 data. *International Journal of Climatology*. doi: 10.1002/joc.6669
900 Zika, J. D., Skliris, N., Nurser, A. J. G., Josey, S. A., Mudryk, L., Laliberte, F.,
901 & Marsh, R. (2015). Maintenance and broadening of the ocean's salinity dis-
902 tribution by the water cycle. *Journal of Climate*, 28(24), 9550–9560. doi:
903 10.1175/JCLI-D-15-0273.1
904 Zingone, A., D'Alelio, D., Mazzocchi, M. G., Montresor, M., & Sarno, D. (2019,
905 05). Time series and beyond: Multifaceted plankton research at a marine
906 mediterranean lter site. *Nature Conservation*, 34, 273–310. doi: 10.3897/
907 natureconservation.34.30789

Supporting Information for ”Microstructure observations of the summer-to-winter destratification at a coastal site in the Gulf of Naples”

Florian Kokoszka¹, Fabio Conversano¹, Daniele Iudicone¹, Bruno Ferron²,

Pascale Bouruet-Aubertot³, Justine Mc Millan⁴

¹Stazione Zoologica Anton Dohrn, Naples, Italy

²Univ. Brest, CNRS, IFREMER, IRD, Laboratoire d’Océanographie Physique et Spatiale (LOPS), IUEM, Plouzané, France

³Sorbonne Université (UPMC, Univ Paris 06)-CNRS-IRD-MNHN, LOCEAN, Paris, France

⁴Rockland Scientific International Inc., Victoria, Canada

Contents of this file

1. Text for supplementary tables S1 and S2
2. Text for supplementary figures S1 to S5
3. Table S1 and S2
4. Figures S1 to S5

Introduction We provide in Tab. S1 the list and dates of the CTD casts (referenced as MC), including the sequence of VMP profiles. Statistics of the Turners’s regimes by layers

Corresponding author: F. Kokoszka, Department of Research Infrastructures for Marine Biological Resources (RIMAR), Stazione Zoologica A. Dohrn, villa Comunale, 80121, Naples, Italy (florian.kokoszka@szn.it)

are given in Tab. S2. We provide in Fig. S1 some details of the VMP data processing. The stratification's decomposition through baroclinic modes of internal waves is presented in Fig. S2. Vertical profiles of some MC casts for CTD and VMP data are detailed in Fig. S3. Additional statistics of the Sh_{LP} are presented in Fig. S4 and Fig. S5.

Tab S1. Metadata We present in Tab. S1 the dates and references of CTD and VMP profiles.

Tab S2. Turner's regimes We present in Tab. S2 some statistics from the Turner's analysis.

Fig S1. VMP processing We calculated dissipation rates of turbulent kinetic energy with the ODAS Toolbox provided by Rockland (version 4.4.06). We present on Fig. S1 the quality metric of our data with the Figure of Merit (FM) and two examples of Nasmyth's fit illustrating stratified and weakly stratified water-column cases.

Fig S2. Stratification and baroclinic modes of internal waves Ocean dynamic vertical modes were calculated for each profile from N^2 , using the routine from Klink (1999). Profiles were smoothed by filtering over a 10m-length running window before applying the algorithm. We focused then on the two first modes B1 and B2 that presented the largest variances. We defined then some vertical envelopes for the layers of these two modes. For each profile, we considered the layer containing the shear maxima of the first two baroclinic modes. To achieve this, we normalized the shear maxima to 1 and identified the depths interval, as the upper and lower depths of the layer where values were > 0.9 . To consider only stratified part of the water-column, calculations were made below the MLD. A comparison between N^2 calculated from both VMP-microCT and CTD hydrology, with a plot of the baroclinic modes and their envelope is shown on Fig. S2.

Fig S3. VMP casts's examples We present on Fig. S3 vertical profiles from the VMP casts MC1173, MC1175 and MC1180 to show some examples of the rich structure of the water-column. Cast MC1180 illustrates a winter case when the MLD reaches the proximity of the bottom layer, where a turbid feature is present from 62 to 70m. In the stratified cases of casts MC1173 and MC1175, even more thin, turbid bottom layers are present too below 60m. Weak double salt fingering layers can be seen too, below the MLD between 25 and 45m, with Tu angles around 60° and 50° , respectively. All casts show intensified Sh_{LP} located below the passage of the local density gradients.

Fig S4. Probability density functions of the low-frequency content of the micro-structure shear The stratified layers possibly containing internal wave activity were remarkably co-located with the low-passed energy component Sh_{LP} (see Appendix) that could be an interesting proxy of energetic motions, even its values are not possible to interpret. A clear pattern is visible (see Fig. A1), with intense occurrences distributed into the highly stratified layers during the summer period, and then into the subsurface layers marking the baroclinic modes $B1$ and $B2$. Two tendencies are visible. A first one below the MLD and $B1$ in July and early August, and a second one through both $B1$ and $B2$ layers from mid-August to the end of October. In terms of distribution (Fig. S4), the most intense values of around $1 \times 10^{-3} \text{ s}^{-2}$ are contained into the bins below the MLD in the $B1$ bin (Fig. S4.b). Surface layers are dominated by weaker values of around $6 \times 10^{-2} \text{ s}^{-2}$ (Fig. S4.a).

Fig S5. Dissipation rates in function of N^2 and Sh_{LP} Even Sh_{LP} is challenging to use and interpret, a classical display averaged values of ϵ ($W.kg^{-1}$) by intervals ΔN^2 (s^{-2}) and ΔSh_{LP} (s^{-2}) is shown on Fig. S5.

Table S1. General information of the MC-CTD casts and VMP profiles.

| VMP# | CTD# (MC cast) | Date | VMP# | CTD# (MC cast) | Date | VMP# | CTD# (MC cast) | Date |
|------|-------------------|------------------|------|-------------------|------------------|------|-------------------|------------------|
| 1 | 1160 | 07/07/2015 08:01 | 24 | 1168 | 01/09/2015 07:46 | 47 | 1176 | 03/11/2015 09:31 |
| 2 | 1161 | 15/07/2015 09:39 | 25 | 1168 | 01/09/2015 08:40 | 48 | 1177 | 10/11/2015 09:24 |
| 3 | 1161 | 15/07/2015 09:41 | 26 | 1168 | 01/09/2015 08:43 | 49 | 1177 | 10/11/2015 09:27 |
| 4 | 1162 | 21/07/2015 08:04 | 27 | 1169 | 08/09/2015 07:57 | 50 | 1178 | 18/11/2015 09:23 |
| 5 | 1162 | 21/07/2015 08:07 | 28 | 1169 | 08/09/2015 08:00 | 51 | 1178 | 18/11/2015 09:25 |
| 6 | 1162 | 21/07/2015 08:55 | 29 | 1169 | 10/09/2015 08:46 | 52 | 1179 | 24/11/2015 09:49 |
| 7 | 1163 | 28/07/2015 08:23 | 30 | 1170 | 16/09/2015 08:27 | 53 | 1179 | 24/11/2015 09:52 |
| 8 | 1163 | 28/07/2015 09:26 | 31 | 1170 | 16/09/2015 08:30 | 54 | 1180 | 01/12/2015 09:08 |
| 9 | 1163 | 28/07/2015 09:29 | 32 | 1170 | 16/09/2015 10:18 | 55 | 1180 | 01/12/2015 09:11 |
| 10 | 1163 | 28/07/2015 08:20 | 33 | 1170 | 16/09/2015 10:21 | 56 | 1181 | 09/12/2015 09:27 |
| 11 | 1164 | 04/08/2015 07:49 | 34 | 1171 | 22/09/2015 07:55 | 57 | 1181 | 09/12/2015 09:30 |
| 12 | 1164 | 04/08/2015 07:51 | 35 | 1171 | 22/09/2015 07:58 | 58 | 1182 | 15/12/2015 09:32 |
| 13 | 1164 | 04/08/2015 08:45 | 36 | 1171 | 22/09/2015 08:53 | 59 | 1182 | 15/12/2015 09:35 |
| 14 | 1164 | 04/08/2015 08:48 | 37 | 1171 | 22/09/2015 08:56 | 60 | 1183 | 22/12/2015 09:01 |
| 15 | 1165 | 11/08/2015 08:11 | 38 | 1172 | 08/10/2015 08:38 | 61 | 1183 | 22/12/2015 09:04 |
| 16 | 1165 | 11/08/2015 08:14 | 39 | 1172 | 08/10/2015 08:40 | 62 | 1184 | 29/12/2015 09:01 |
| 17 | 1166 | 18/08/2015 07:55 | 40 | 1173 | 13/10/2015 08:21 | 63 | 1184 | 29/12/2015 09:04 |
| 18 | 1166 | 18/08/2015 07:58 | 41 | 1173 | 13/10/2015 08:24 | 64 | 1186 | 19/01/2016 08:36 |
| 19 | 1167 | 26/08/2015 07:34 | 42 | 1174 | 22/10/2015 08:09 | 65 | 1186 | 19/01/2016 08:39 |
| 20 | 1167 | 26/08/2015 07:37 | 43 | 1174 | 22/10/2015 08:12 | 66 | 1187 | 26/01/2016 09:59 |
| 21 | 1167 | 26/08/2015 08:59 | 44 | 1175 | 27/10/2015 09:34 | 67 | 1187 | 26/01/2016 10:02 |
| 22 | 1167 | 26/08/2015 09:02 | 45 | 1175 | 27/10/2015 09:37 | 68 | 1188 | 02/02/2016 11:29 |
| 23 | 1168 | 01/09/2015 07:44 | 46 | 1176 | 03/11/2015 09:28 | 69 | 1188 | 02/02/2016 11:32 |
| | | | | | | 70 | 1190 | 23/02/2016 10:19 |
| | | | | | | 71 | 1190 | 23/02/2016 10:22 |

Table S2. (a) Decibar occupation of the Turner’s regimes for the whole dataset. (b) Statistics by layers and period bins for the double diffusive and (c) diffusive convection regimes.

(a) General

| Regime | SF | Stable | Diffusive | Instable | All |
|--------|-------|--------|-----------|----------|------|
| Count | 1202 | 2159 | 396 | 142 | 3899 |
| % | 30.8% | 55.4% | 10.2% | 3.6% | 100 |

(b) Double diffusive regime (salt fingers)

| Bin | % | mean Tu mean R_ρ | median | std | SF% | Stable% | Diff.% | Inst.% | Bin count |
|-------------|-----|------------------------------------|--------------|--------------|-------|---------|--------|--------|-----------|
| All | 100 | 54.7 (Tu) 8.88 (R_ρ) | 51.8 6.79 | 9.3 6.82 | 30.80 | 55.4 | 10.2 | 3.6 | 3899 |
| surface-MLD | 32 | 60.5 6.03 | 58.7 3.77 | 11.2 5.67 | 24.7 | 41.8 | 25 | 8.5 | 1573 |
| MLD-bottom | 68 | 52.1 10.4 | 50.2 8.36 | 6.61 6.89 | 35 | 64.6 | 0.1 | 0.3 | 2326 |
| W1 | 13 | 59.8 6.07 | 58.7 3.88 | 10.4 5.54 | 28.1 | 46.2 | 22.7 | 3 | 572 |
| W2 | 19 | 61.0 6.01 | 58.4 3.69 | 11.8 5.77 | 22.8 | 39.3 | 26.3 | 11.7 | 1001 |
| B1 | 39 | 51.5 10.5 | 50.3 8.57 | 5.34 6.59 | 59.9 | 39.3 | 0.4 | 0.4 | 778 |
| B2 | 13 | 53.4 10.1 | 50.5 7.82 | 8.97 7.67 | 29.6 | 69.5 | 0 | 0.9 | 544 |
| BBL | 6 | 55.02 8.67 | 52.4 5.79 | 8.46 6.43 | 8.8 | 90.9 | 0.2 | 0 | 803 |

(c) Diffusive regime (convection)

| Bin | % | mean Tu mean R_ρ | median | std | SF% | Stable% | Diff.% | Inst.% | Bin count |
|-------------|-----|-------------------------------------|----------------|---------------|-------|---------|--------|--------|-----------|
| All | 100 | -67.4 (Tu) 0.43 (R_ρ) | -67.9 0.42 | 11.9 0.25 | 30.8 | 55.4 | 10. | 3.6 | 3899 |
| surface-MLD | 99 | -67.57 0.43 | -68.1 0.42 | 11.8 0.25 | 24.7 | 41.8 | 25 | 8.5 | 1573 |
| MLD-bottom | 1 | -49.3 0.07 | -49.1 0.07 | 3.4 0.06 | 35 | 64.6 | 0.1 | 0.3 | 2326 |
| W1 | 33 | -63.6 0.35 | -63.0 0.32 | 10.04 0.20 | 28.1 | 46.2 | 22.7 | 3 | 572 |
| W2 | 66 | -69.50 0.48 | -71.25 0.49 | 12.21 0.26 | 22.80 | 39.30 | 26.30 | 11.70 | 1001 |
| B1 | 1 | -66.8 0.42 | -76.2 0.60 | 17.6 0.34 | 59.9 | 39.3 | 0.4 | 0.4 | 778 |
| B2 | 0 | NaN NaN | NaN NaN | NaN NaN | 29.6 | 69.5 | 0 | 0.9 | 544 |
| BBL | 1 | -47.6 0.04 | -47.6 0.04 | 2.14 0.03 | 8.8 | 90.9 | 0.2 | 0 | 803 |

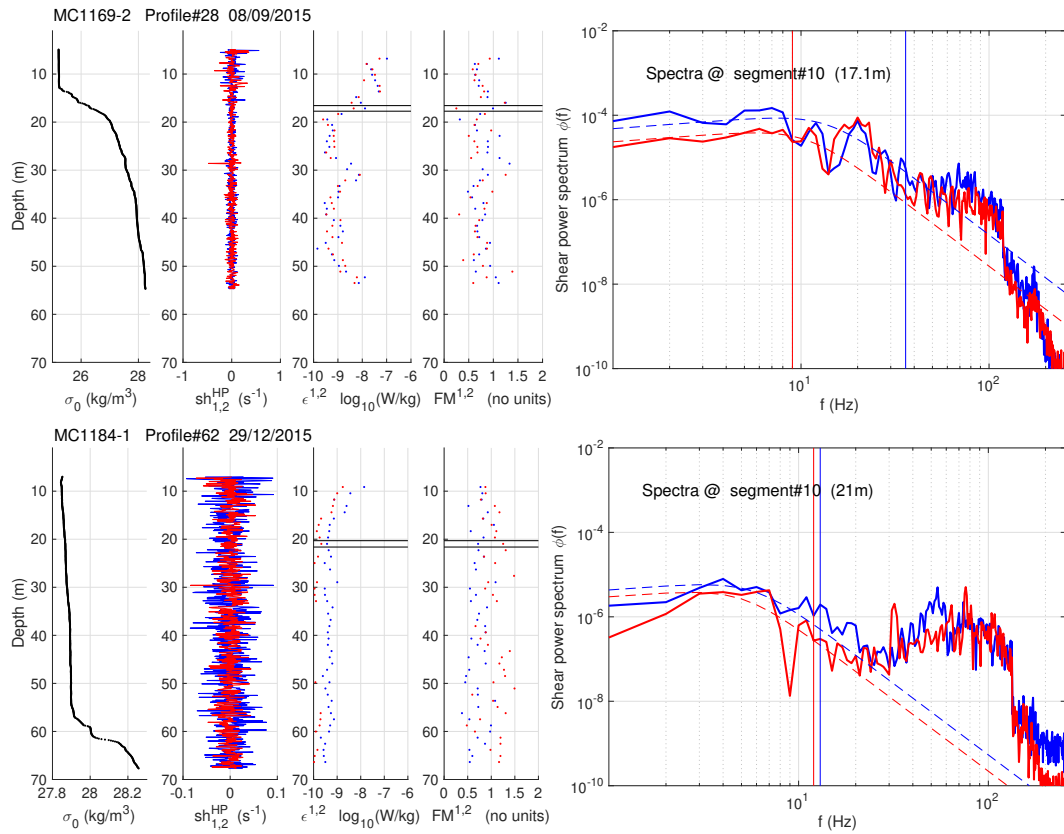


Figure S1. Examples of Nasmyth's spectra fits, for stratified (top) and weakly stratified cases (bottom). The final ϵ is the mean value of the individual estimates ϵ_1 and ϵ_2 , excepted for the case where only one value is available (for example after rejection if $FM > 1.5$). Finally, if two estimates differ by one order of magnitude, the lowest is kept.

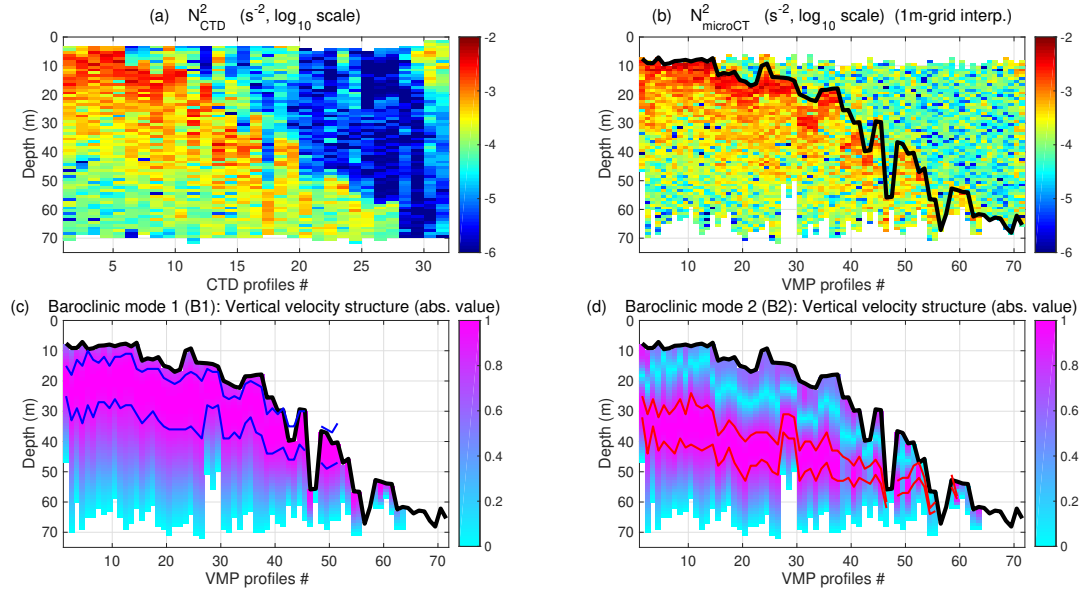


Figure S2. (a) Profiles of the Brunt-Väisälä frequency N_{ctd}^2 (s^{-2}) computed from the hydrology obtained with the CTD Seabird 911+ and (b) N_{vmp}^2 (s^{-2}) computed from the hydrology obtained with the micro-CT nose-mounted on the VMP-250. Both quantities have been calculated with the dedicated Gibbs Seawater function. $MLD_{0.4^\circ}^\theta$ is shown in thick black. (c) Vertical velocity structure (non-dimensional) of the first and (d) second baroclinic modes calculated from N_{vmp}^2 . $MLD_{0.4^\circ}^C$ (thick black line), region of maximum energy of baroclinic mode 1 (between blue lines) and mode 2 (between red lines).

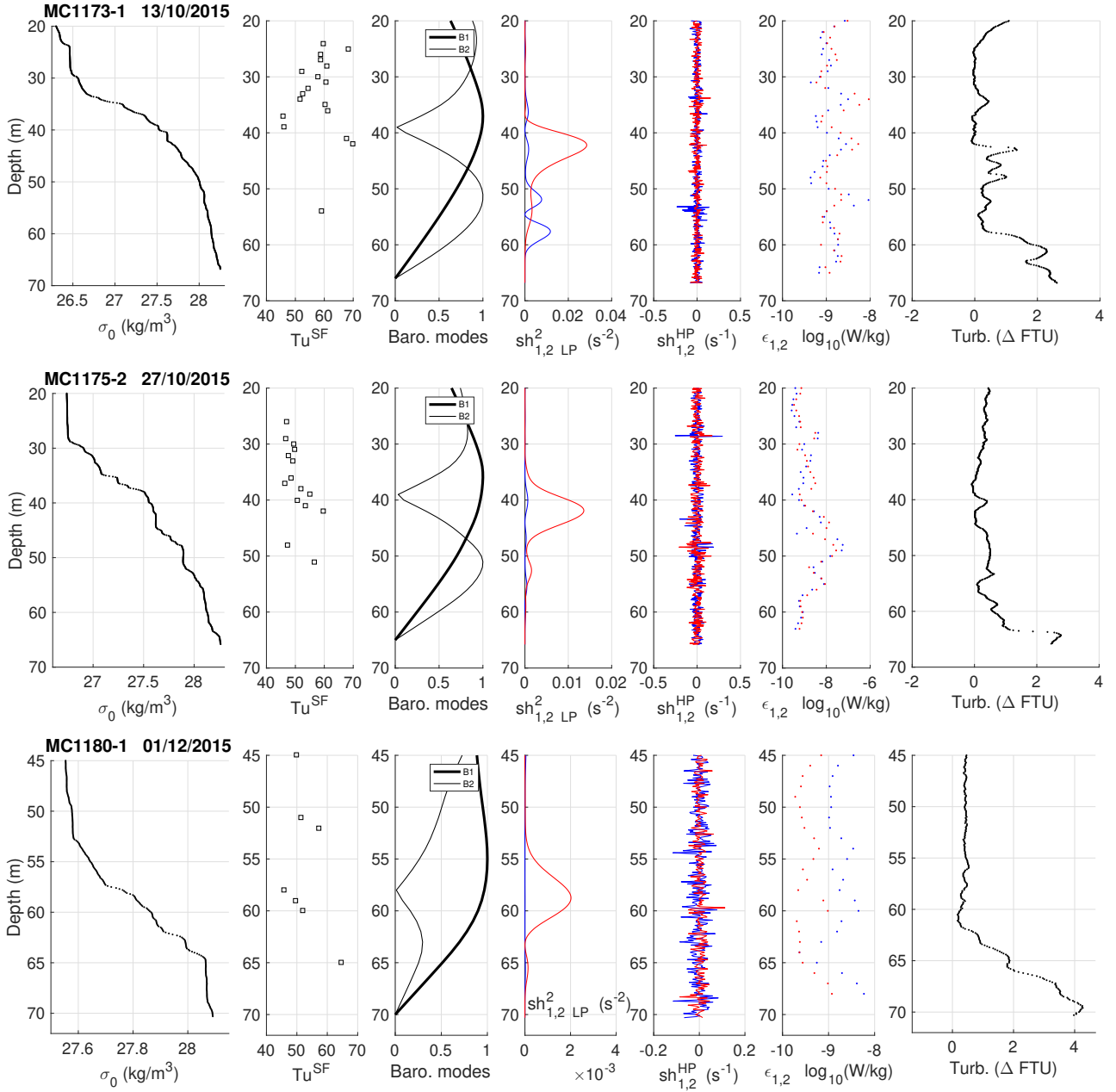


Figure S3. Top to bottom : profiles from the VMP casts MC1173, MC1175 and MC1180. From left to right : σ_0 (kg m^{-3}), Turner angles ($^\circ$) into the salt-fingering regime, first and second vertical baroclinic modes (non-dimensional), low-passed energy shears Sh_{LP} (s^{-2}), hi-passed shears (s^{-1}) used to estimate ϵ (W kg^{-1}), and turbidity (ΔFTU , offset from the reference value -2.5). For shears and ϵ , blue and red refers to the respective shear probes 1 and 2.

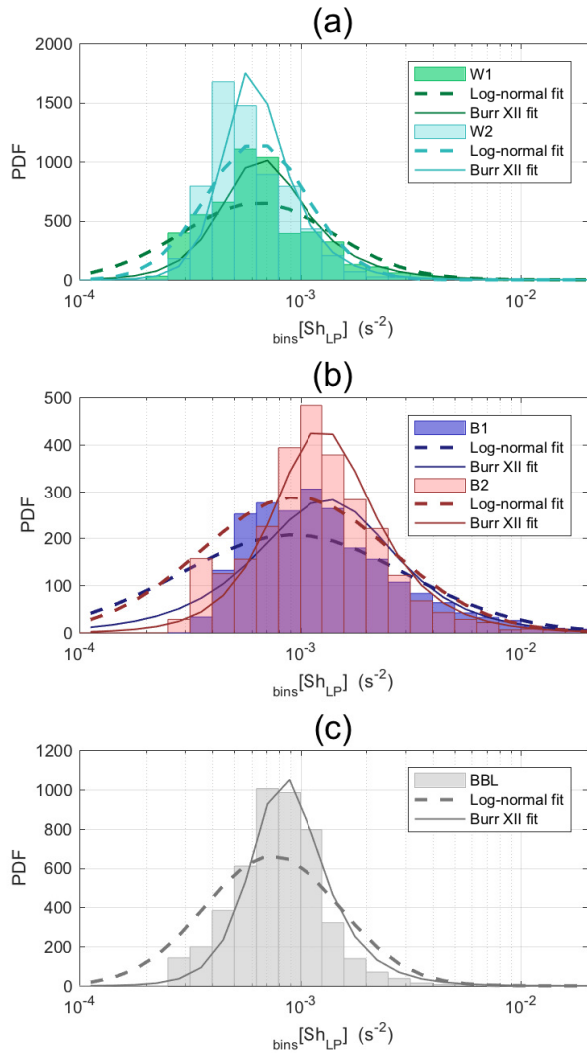


Figure S4. Pdfs of Sh_{LP} i.e. $\langle (\partial_z u)^2 \rangle_{LP}^{3m} (s^{-2})$ through (a) temporal bins W1 and W2, and (b,c) vertical bins B1, B2 and BBL. The fits of the log-normal and Burr type XII distributions are indicated with the dashed and solid lines, respectively.

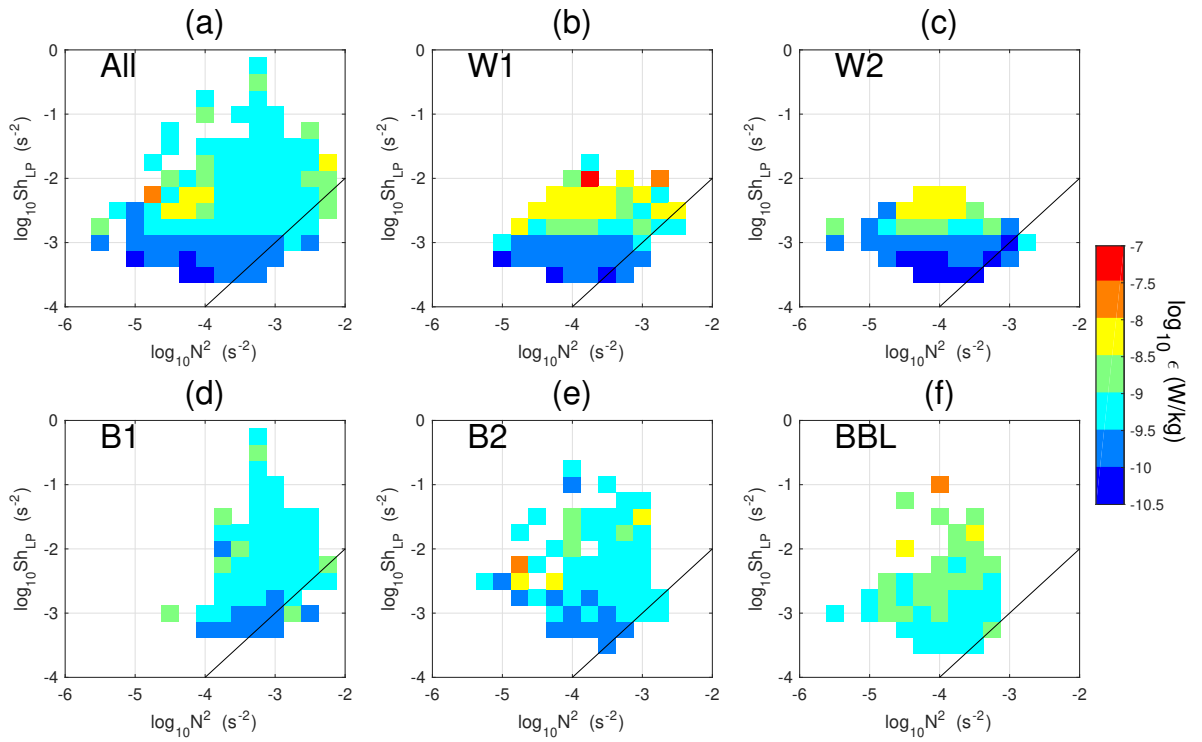


Figure S5. Averaged values of ϵ ($W.kg^{-1}$) by intervals ΔN^2 (s^{-2}) and ΔSh_{LP} (s^{-2}), for the different groups of periods and layers. Intervals ΔN^2 and ΔSh_{LP} have been defined = 0.25 in the logarithmic domain (log_{10}). Black line indicates $\frac{N^2}{Sh_{LP}} = 1$.